Journal of the European Ceramic Society 37 (2017) 427–440

Contents lists available at www.sciencedirect.com

Journal of the European Ceramic Society

journal homepage: www.elsevier.com/locate/jeurceramsoc

Review article

Crystal chemistry, stability and properties of interlanthanide perovskites: A review

Cristina Artini [a,b,*]

[a] DCCI, Department of Chemistry and Industrial Chemistry, University of Genova, Via Dodecaneso 31, 16146 Genova, Italy
[b] CNR-ICMATE, Via De Marini 6, 16149 Genova, Italy

ARTICLE INFO

Article history:
Received 3 May 2016
Received in revised form 30 August 2016
Accepted 31 August 2016
Available online 5 September 2016

Keywords:
Perovskites
Phase transformations
Magnetic properties
Optical properties
Protonic conductors

ABSTRACT

In this review structural features, stability issues and physical properties of the eleven interlanthanide perovskites prepared at atmospheric pressure are surveyed and discussed. Due to the reduced size difference between cations, the structure of these oxides is strongly distorted with respect to the ideal cubic case. Therefore, in structure maps they are located close to the boundary of the perovskitic stability field; an interesting correlation between stability and the Goldschmidt tolerance factor *t* shows that the perovskitic temperature range narrows with decreasing *t*. Magnetic and optical properties are strictly related to the presence of 4*f* electrons, that determine the existence of many discrete energy levels. Acceptor-doped $LaYO_3$ and $LaYbO_3$ are comparable in terms of protonic conductivity to the well known cerates, and thanks to their better chemical stability against CO_2, they are a good alternative to the latter in solid oxide fuel cells. The high dielectric constant of some interlanthanide perovskites makes them interesting candidates as gate oxides in MOSFETs.

Contents

* Corresponding author at: DCCI, Department of Chemistry and Industrial Chemistry, University of Genova, Via Dodecaneso 31, 16146 Genova, Italy.
E-mail addresses: artini@chimica.unige.it, c.artini@ge.ieni.cnr.it

http://dx.doi.org/10.1016/j.jeurceramsoc.2016.08.041
0955-2219/

1. Introduction

Perovskites form one of the widest and most commonly encountered structural families in solid state chemistry. Due to the ability of this structure to accommodate a large number of cations as well as of anions, and to tolerate distortions and non-stoichiometry, to this class belong compounds characterized by a wide variety of properties, such as superconductivity [1], ionic conductivity [2–4], protonic conductivity [5] piezoelectricity [6], ferroelectricity [7], colossal magnetoresistance [8], photoluminescence [9] and catalytic activity [10]. Even if the majority of perovskites can be well described by the formula ABO_3, being A and B metal ions, also fluorides [11], nitrides [12], oxynitrides [13] and hydrides [14] can crystallize in this structural form, giving rise to a huge and highly heterogeneous class of compounds.

Within this wide framework, interlanthanide perovskites form a small family of eleven mixed oxides reported for the first time in the Sixties of last century by Schneider et al. [15] and Müller-Buschbaum et al. [16,17]. In structure maps they are located at the boundary of the perovskitic existence field due to the reduced size difference between A and B ions with respect to the ideal cubic case; for this reason, from the viewpoint of basic science, they are an interesting example of the flexibility of this atomic arrangement, that can undergo heavy structural deformations to compensate for dimensional misfit: indeed, these compounds offer an ideal opportunity for the investigation of the perovskitic formability.

The presence of the deep-lying 4*f* electrons of both rare earth ions, screened by outer electrons, strongly determines two of the most remarkable physical properties of interlanthanide perovskites, namely the magnetic [18] and optical [19] ones; moreover, several interlanthanide perovskites doped by bivalent ions, are good proton conductors [20,21] with potential applications in solid oxide fuel cells (SOFC's) [22] and as catalysts [10]. Nevertheless, despite their appealing features, only few fundamental studies on magnetism, and in general on physical properties of these compounds, appeared in the literature for quite a long time; after the thorough investigations carried out in the Seventies of last century, in fact, studies on these oxides were almost abandoned, and only recently this and other research groups undertook investigations about synthesis, stability and structural and magnetic properties of these oxides [23–29]. Properties of proton conduction, on the contrary, received attention since their discovery in these perovskites [30].

Extensive reviews have been devoted to the most appealing properties and applications of perovskites [31–33], double perovskites [34], and lanthanide-containing perovskites [35], but to the Authors' knowledge investigations performed on interlanthanide perovskites have not ever been collected and systematized. Thus, in this work a structural survey of interlanthanide perovskites is provided, with special reference to the formability likelihood of the distorted orthorhombic structure, to structure maps and to the effect of temperature and composition on the perovskitic stability; a paragraph is devoted to the Goldschmidt tolerance factor *t*, with the aim to clear up the misleading that can arise from the use of different ionic radii. In section 3 the synthetic methods adopted for the preparation of both monocrystals and polycrystalline samples, as well as of thin films, are described; finally, in section 4 physical properties are reviewed, in particular optical and magnetic properties, as well as proton conductivity; high-*k* dielectrics applications of $LaYbO_3$ and $LaLuO_3$ are mentioned too.

2. Stability of interlanthanide perovskites

2.1. The perovskitic structure and the Goldschmidt tolerance factor t

A very large number of mixed oxides with general formula ABO_3 crystallize in one of the perovskitic structural types; in the ideal case the cell is cubic and belongs to the $Pm\bar{3}m$ space group (isotypic crystal: $SrTiO_3$), with A in twelvefold and B in octahedral coordination towards oxygen, as depicted in Fig. 1, where BO_6 octahedra are highlighted. Atoms are located in three atomic sites, namely A in 1*b* (1/2, 1/2, 1/2), B in 1*a* (0, 0, 0) and O in 3*d* (1/2, 0, 0). Nevertheless, this event occurs only for few compounds, since a rigid size correlation among the three atomic species is necessary to avoid symmetry-lowering distortions. The great majority of perovskitic oxides, on the contrary, presents a structural distortion consisting either in a cation displacement or in a tilting of the BO_6 octahedra; while the cation displacement only produces a distortion in the BO_6 polyhedra, the octahedral tilting can be described through a complex model consisting in many tilt systems. Since it has a direct consequence on the lattice parameters, it has been thoroughly investigated [36–38], and all the experimentally observed octahedral tilts were collected and systematized into two different notations, introduced by Glazer [39] and Aleksandrov [40]; following the Glazer's notation, 23 possible tilt systems belonging to 15 different space groups were recognized.

The eleven interlanthanide perovskites $LaREO_3$ synthesized at atmospheric pressure (RE≡Y, Ho-Lu), $CeREO_3$ (RE≡Tm-Lu) and $PrREO_3$ (RE≡Yb-Lu), as well as $NdLuO_3$, obtainable in the perovskitic form at high pressure, crystallize in the most commonly found distortion of the perovskitic structure, namely the orthorhombic one, belonging to the *Pnma* space group (isotypic crystal: $GdFeO_3$). Actually, the symmetry of some interlanthanide perovskites, such as for instance $LaYbO_3$, was in the past a matter of debate in the literature, due to their possible attribution to the non-centrosymmetric space group $Pna2_1$ [41], as well as to *Cmcm* [42], subsequently corrected into the aforementioned *Pnma*. Due to their atomic arrangement, interlanthanide perovskites can be classified in the *a-b+a-* tilt system, according to the Glazer's notation. The latter notation means that the BO_6 octahedra are rotated by an angle *a* around the *x* and *z* axes and by an angle *b* around the *y* axis of the aristotype cubic coordinate system, with signs indicating the in-phase (+) and out-of-phase (−) sense of rotation of neighbouring octahedra. Fig. 2 shows the view along the [−101] direction, corresponding to the *c* axis of the aristotype cubic structure of an

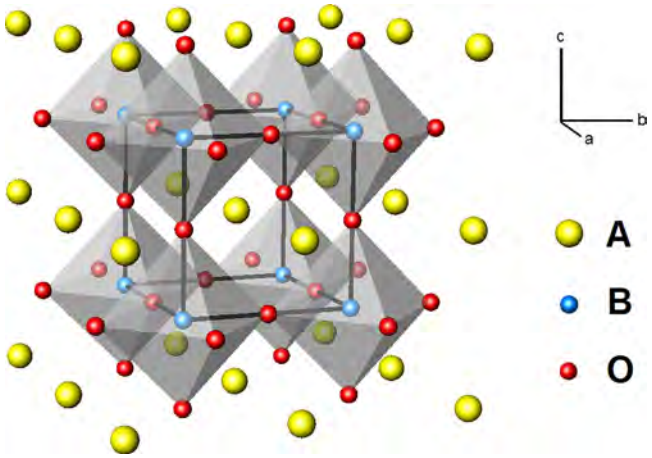

Fig. 1. Representation of the ideal cubic ($Pm\bar{3}m$) perovskitic structure.

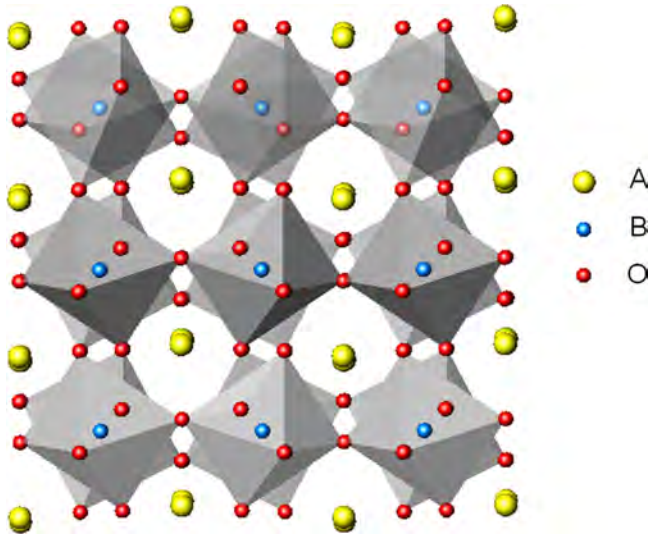

Fig. 2. View along the [−101] direction, corresponding to the *c* axis of the cubic aristotype structure for a generic *a*-*b*+*a*- tilted perovskite.

interlanthanide perovskite: the out-of-phase alignment is evident. By applying the *a*-*b* + *a*-tilting to the cubic perovskite, symmetry is lowered, and a rearrangement of the oxygen position takes place, with the consequent generation of two different atomic sites for this atom, namely the 8*d* (O1) and 4*c* (O2). As a consequence, the coordination polyhedron of oxygen around A changes from a cubo-octahedron (CN: 12) to a square antiprism (CN: 8) [CN: coordination number]; the tilted octahedron built around B, on the contrary, is essentially a regular one. The aforementioned modifications with respect to the ideal case allow to have the optimal fit of A cations at the cubo-octahedral sites. In fact, in the case of interlanthanide perovskites the A ionic radius is too small if compared to the B and the oxygen size, to guarantee the stability of a cubic perovskite.

The closeness of a certain perovskite to the ideal structure is ruled by dimensional issues, and it is measured by the Goldschmidt tolerance factor *t* [43], a geometric factor that accounts for the fitting of the A cation to the undistorted cubic cell. When the calculation employs ionic radii, *t* is generally named t_{IR}, and it is defined as

$$t_{IR} = (R_A + R_O)/\sqrt{2}(R_B + R_O) \quad (1)$$

where R_A, R_B and R_O are the A, B and oxygen ionic radii, respectively.

At this stage, it is worth to underline that misleading discrepancies can be found between t_{IR} values calculated by using ionic radii with CN 6 or 12 for the A cation. In particular, CN 6 is historically used for both A and B cations, even if A is coordinated to 12 oxygen atoms. This choice, that corresponds to ignore the effect of the coordination number on the *t* factor, is sometimes justified by the unavailability of several ionic radii with CN 12: some of them are in fact lacking in the Shannon's systematic study [44], while all the older Ahrens' radii [45] are reported only with CN 6. Nevertheless, the so performed t_{IR} calculation provides values that reflect an unrealistic scenario. The use of Shannon ionic radii with CN 6 for the A cation gives the traditional perovskitic range for t_{IR} ranging between 0.75 and 1 [35]; moreover, a minimum value of 0.77 is assessed by Schneider and Roth [46], who employ Ahrens' radii [45], and hence CN 6 for both cations; more recently, the lowest limit is set at t_{IR} = 0.78 by Randall et al. [47]. At variance with the aforementioned works, CN 12 is employed for the A cation by the program code SPuDS, aimed at the prediction of the perovskitic stability [48]; recently, this and other research groups adopted the latter option for the computation of t_{IR} values of interlanthanide perovskites [27,29].

In order to avoid ambiguities, as well as to bypass the unavailability of some ionic radii with the desired coordination number, it is in some cases more convenient to calculate *t* on the basis of the bond valence method, as follows:

$$t_{BV} = d_{A-O}/\sqrt{2}d_{B-O} \quad (2)$$

where d_{A-O} and d_{B-O} are the A–O and B–O interatomic distances, respectively; they result from the average A–O and B–O distances calculated over a large number of experimental values [49,50]. In Table 1 room temperature t_{IR} values, calculated by considering the A cation both with CN = 6 ($t_{IR,CN6}$) and CN = 12 ($t_{IR,CN12}$), as well as t_{BV} values, are reported for sake of comparison for the eleven interlanthanide perovskites and for a group of eleven interlanthanide non perovskitic ABO_3 oxides. It can be noticed that at each composition t_{BV} is much closer to $t_{IR,CN12}$ than to $t_{IR,CN6}$; moreover, for each composition $t_{IR,CN12}$ is higher than t_{BV}. Zhang et al. [51] recently systematized the formability likelihood of ABO_3 perovskites through the employment of the bond valence method using the software SPuDS [48]; they formulated an empirical expression obtained from an assessment over 376 ABO_3 compounds, correlating Shannon's $t_{IR,CN12}$ and t_{BV} values:

$$t_{BV} = 1.015t_{IR,CN12} - 0.015 \quad (3)$$

According to data reported in Table 1, the perovskite/non perovskite boundary for interlanthanide $t_{IR,CN12}$~0.847 oxides could be set at $t_{IR,CN6}$~0.745 and $t_{IR,CN12}$~0.847. In terms of t_{BV}, on the contrary, the limit is located at ~0.822, in excellent agreement with data reported in [51] for $A^{3+}B^{3+}O_3$ mixed oxides. In this work, t_{IR} is always meant as $t_{IR,CN12}$, unless differently specified.

With regard to the meaning of the Godlschmidt factor, values of *t* close to 1 correspond to the ideal cubic structure, while the lower is *t*, the more distorted is the perovskitic cell; below a certain *t* value, the structural distortion is no more sufficient to guarantee the phase stability, and a more favourable atomic arrangement sets in. In particular, non-perovskitic ABO_3 interlanthanide oxides crystallize in one of the possible structural forms typical of rare earth sesquioxides, namely in the A [hexagonal, space group: $P\bar{3}m1$, isotypic crystal: La_2O_3], B [monoclinic, space group: $C2/m$, isotypic crystal: Sm_2O_3] and C [cubic, space group: $Ia\bar{3}$, isotypic crystal: $(Mn_{0.5}Fe_{0.5})_2O_3$] structure, according to the average cationic radius [52]. Owing to the small size difference between A and B, interlanthanide perovskites show a low value of the *t* factor. Taking into account the non existence of the perovskitic form of $LaDyO_3$ (t_{IR} = 0.8441), $LaHoO_3$ (t_{IR} = 0.8482) can be regarded as the end member of the series, and it can be concluded that interlanthanide perovskites are located close to the boundary of the perovskitic stability field.

As expected, lattice parameters regularly vary as a function of the A and B sizes. In Fig. 3 the volume cubic root calculated from data reported in [18,53] is shown as a function of t_{IR}; data related to $NdLuO_3$ are included too, even if the cited mixed oxide is generally considered metastable in the perovskitic form, as explained later. It can be noticed that data roughly align in series, according to the identity of the A either the B cation, in agreement with the dependence of the Goldschmidt *t* factor on the size of the B atom. Only $LaYO_3$ appears not to follow the trend of other La-based perovskites: even if generally included into the family of interlanthanide perovskites, it differs from the other members due to the presence of Y, that does not possess any *f* electron; this different electronic feature can influence even the cell dimension, despite the closeness of the Y^{3+} size to the one of other trivalent rare earths. It can also be observed that Pr-based perovskites seem to contradict the behaviour shown by all the other compositions, as they present an increase in the volume cubic root with increasing the t_{IR} value. This anomaly can be ascribed to the fact that t_{IR} of $PrYbO_3$ and $PrLuO_3$ are calculated starting from the correspond-

Table 1
Room temperature $t_{IR,CN6}$, $t_{IR,CN12}$ and t_{BV} values for interlanthanide perovskites and for eleven non-perovskitic interlanthanide ABO_3 oxides.

Perovskites composition	$t_{IR,CN6}$	$t_{IR,CN12}$	t_{BV}	Non-perovskites composition	$t_{IR,CN6}$	$t_{IR,CN12}$	t_{BV}
$LaLuO_3$	0.7615	0.8632	0.8523	$LaDyO_3$	0.7445	0.8465	0.8410
$LaYbO_3$	0.7592	0.8605	0.8546	$CeErO_3$	0.7448	0.8485	0.8393
$PrLuO_3$	0.7482	–	0.8415	$CeHoO_3$	0.7412	0.8444	0.8256
$CeLuO_3$	0.7545	0.8569	0.8457	$CeDyO_3$	0.7376	0.8403	0.8344
$LaTmO_3$	0.7551	0.8560	0.8414	$PrTmO_3$	0.7418	–	0.8307
$CeYbO_3$	0.7522	0.8543	0.8479	$PrErO_3$	0.7385	–	0.8352
$LaErO_3$	0.7517	0.8522	0.8459	$PrHoO_3$	0.7349	–	0.8216
$CeTmO_3$	0.7481	0.8498	0.8348	$PrDyO_3$	0.7314	–	0.8304
$LaYO_3$	0.7484	0.8485	0.8343	$NdLuO_3$	0.7459	0.8373	0.8311
$LaHoO_3$	0.7481	0.8482	0.8322	$NdYbO_3$	0.7436	0.8347	0.8333
$PrYbO_3$	0.7458	–	0.8438	$NdDyO_3$	0.7292	0.8185	0.8200

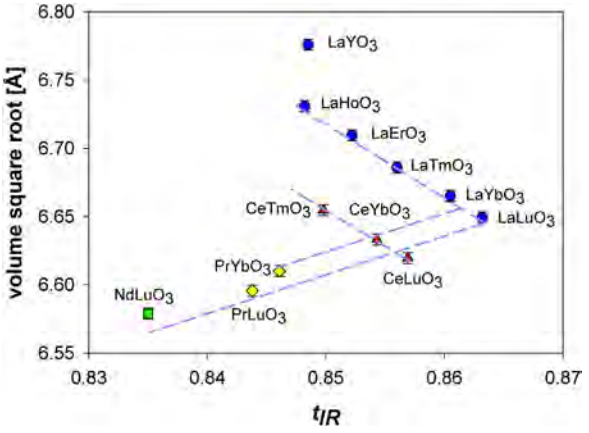

Fig. 3. Trend of the cell volume square root as a function of t_{IR} for interlanthanide perovskites; dashed lines are a guide for the eye that highlight the linear dependence on t_{IR} of cell volumes related to perovskites sharing the same A or B cation. Data are taken from Refs. [18] and [53].

ing values of t_{BV} through Eq. (3), due to the lack of the Pr^{3+} (CN 12) ionic radius. Therefore, the calculation of t_{BV} is based on the Pr-O, Yb-O and Lu-O distances; since Lu-O (1.971 Å) is reported as a longer distance than Yb-O (1.965 Å) [49,50], t_{BV} results to be higher for $PrYbO_3$ than for $PrLuO_3$, in contradiction with the values of ionic radii ($r_{Lu3+,CN6}$ = 0.977 Å, $r_{Yb3+,CN6}$ = 0.985 Å). This example highlights that the employ of t_{BV} values is very useful in case of non availability of ionic radii; nevertheless, data have to be carefully treated, since interatomic distances are generally known with a lower accuracy with respect to ionic radii. Moreover, Eq. (3) is a general expression formulated taking into account a large number of perovskites having t values that span over the entire range, so that the application to any particular case can be susceptible to a certain error.

2.2. Interlanthanide perovskites and structure maps

Structure maps are a powerful tool for the structural prediction based on the assessment of the existence field of a certain crystallographic arrangement as a function of chosen parameters; moreover, they provide useful hints to discuss the occurrence of structural regions within phase diagrams. While originally employed for the prediction of intermetallics structures by means of different methods [54–56], if properly modified they can be used even for oxides, and in particular for perovskites. Several approaches have been attempted for the prediction of perovskites formability, resulting in structure maps based on ionic radii [57], octahedral factors [58], bond valence factors [51], or on a modification of the method relying on ionic radii obtained by introducing bond ionicities [59].

The approach introduced by Roth [57], based on ionic radii, is the simplest way to separate properties deriving from the A and the B cation; it consists in drawing a diagram reporting the existence fields of perovskitic and non perovskitic oxides as a function of the A and B cationic sizes (on the x and y axis, respectively). Ionic radii used by Roth are taken from Shannon [44] and consider a coordination number of 6 for both cations. A further method based just on dimensional parameters, is the one proposed by Li et al. [58], who include also the effect of the oxygen size by reporting the perovskitic stability range as a function of t_{IR} (on the x axis) and the octahedral factor r_B/r_O (on the y axis). A third structure map relying on size factors is the one used by Zhang et al. [51], who propose a modification of the Roth's approach by substituting r_A and r_B by the ideal (A–O) and (B–O) distances, respectively. The concept of ideal bond distance derives from the bond valence model [60,61], that correlates the length of a bond to its strength, and hence the bond length to the valence. The correlation can be described as follows:

$$S_{ij} = exp\left(\frac{R_0 - R_{ij}}{B}\right) \quad (4)$$

where S_{ij} is the bond valence associated to the interaction between the i^{th} and the j^{th} atom, R_{ij} is the i–j bond distance, R_0 is a reference semi-empirical value based on a large number of experimentally determined i–j bond distances [50,61], and B is a constant with typical value of 0.37. The valence of the i^{th} atom can be determined by adding all the individual bond valence contributions S_{ij}:

$$V_i = \sum_j S_{ij} \quad (5)$$

In a perovskite $A^{3+}B^{3+}O_3$, the ideal (A–O) and (B–O) bond distances are the ones that produce $S_{AO} = 0.25$ and $S_{BO} = 0.5$, and consequently a formal valence +3 for both cations (*i.e.* $V_A = 3$ and $V_B = 3$, considering a coordination number of 12 and 6 for A and B, respectively). Noteworthy is that the bond valence model is the theoretical basis for the software codes SPuDS and TUBERS [48].

A structure map that couples dimensional factors to bond ionicities is the one proposed by Giaquinta and zur Loye [59], who plot the (B–O) vs. the (A–O) distance (obtained from the sum of Shannon's radii), multiplied by corresponding the B–O and A–O electronegativity difference, respectively.

Interlanthanide perovskites are generally only partly taken into account in papers that review the formability likelihood of perovskitic ABO_3 oxides according to one of the described methods; sometimes they are not considered at all [58]. Giaquinta and zur Loye [59] and Zhang et al. [51], for example, include some interlanthanide perovskites into their phase diagrams, as well as Bharathy et al. [28]. In the latter work, in particular, a structure map is nicely depicted as a function of the A and B ionic radii, resulting in an interesting representation of the existence fields of interlanthanide ABO_3 oxides crystallizing not only in the perovskitic structure, but also in the aforementioned A, B and C structures.

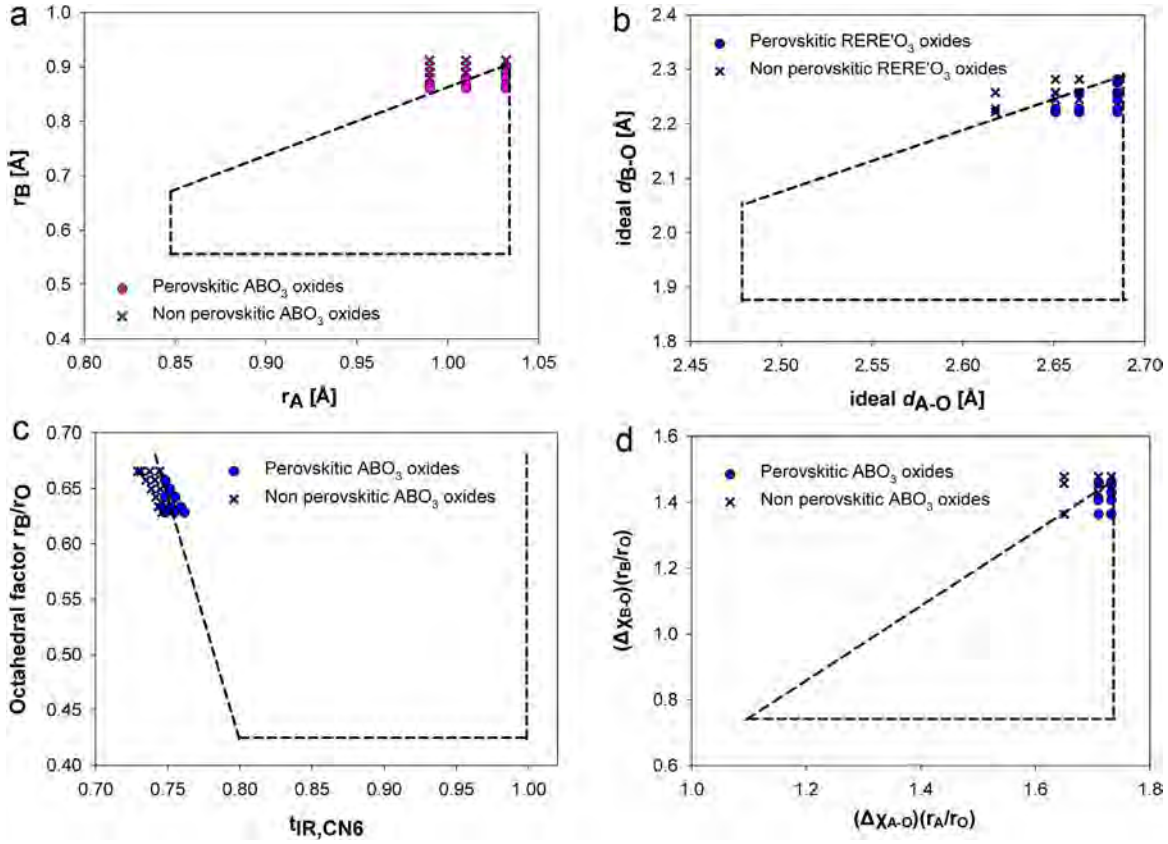

Fig. 4. Structure maps plotted by a) ionic radii; b) ideal bond distances; c) octahedral factor and $t_{IR,CN6}$; d) electronegativity-related parameters. Areas marked by dashed lines are redrawn from references [58,51,59], respectively.

With the aim to analyze the position of interlanthanide perovskites, and to observe the location of the boundary separating perovskitic from non perovskitic oxides, parameters related to all the interlanthanide perovskites, as well as to the eleven non perovskitic interlanthanide ABO_3 oxides reported in Table 1, are introduced into the ionic radii-, ideal distance-, octahedral factor- and bond ionicity-based structure maps reported in the literature; results are represented in Fig. 4a–d, respectively. Moreover, in order to match with the reference structure maps, ionic radii and t_{IR} values used in Fig. 4a–d are referred to coordination number 6 for the A cation. Dashed lines enclose areas where ABO_3 perovskites are reported to exist, according to the corresponding work. It can be observed that in all the structure maps interlanthanide perovskites appear in the closeness of the perovskite/non perovskite boundary, *i.e.* they are located at high values of ionic radii and bond distances, and at low values of t_{IR}. This position reflects the fact that the size of the A cation is close to the highest possible value for the formation of a stable perovskite, and the B cation is almost oversized with respect to A, as testified by the low values of t_{IR}.

2.3. The stability of the perovskitic field as a function of temperature and composition

The stability range of interlanthanide perovskites as a function of both temperature and composition has been especially studied in the Seventies' of last century, and it is reported in a large number of thermal and crystallographic high temperature studies [53,62,63,64–66,67]. According to these studies, the family of interlanthanide perovskites is formed of the eleven aforementioned mixed oxides. The structure of $NdLuO_3$, on the contrary, is quite debated in the literature, since it generally can not be prepared in atmospheric pressure conditions: it could not be obtained at all by Ito et al. [18], while it is elsewhere reported as a mixture of the B and C phases [46,66], containing a certain amount of perovskite [66] depending on the preparation route; on the contrary, the pure perovskitic form was obtained at high-pressure (40 kb) [68], and the compound is generally considered as non thermodynamically stable [66]. Depending on the authors, perovskitic $PrYbO_3$ is considered as a stable [18,65] or a metastable [53] constituent of the Pr–Yb–O system.

Several studies highlight the strict relationship between t and the perovskitic temperature range [23,27]: if formation and decomposition temperatures of the phase are considered, it can be in fact observed that the higher is t, the wider is the temperature range. In other words, the structural closeness to the ideal cubic case is directly related to the phase stability. An explanation of this evidence is reported in [27], where a stability criterion is proposed, derived from geometrical issues affecting the enthalpic and the entropic contribution to the Gibbs free energy of the perovskitic phase. An interesting correlation between thermodynamic data and t values can also be found in [29], where the results of a calorimetric study on the formation enthalpies at room temperature of $LaHoO_3$, $LaErO_3$, $LaTmO_3$ and $LaYbO_3$ are discussed. Data obtained are reported as a function of t_{IR} in Fig. 5: a linear trend can be observed, indicating that the formation of the perovskite becomes more and more exothermic with increasing the t value. If the regression line interpolating experimental points is used to identify the t_{IR} value corresponding to $\Delta H = 0$, and thus to predict the position of the perovskitic boundary, $t_{IR} = 0.8201$ is obtained, *i.e.* a value well below the one related to $LaDyO_3$ (0.8441), that is the highest-t non-perovskitic interlanthanide mixed oxide. This discrepancy is partly recovered if also formation enthalpies of perovskitic $LaMO_3$ (M≡In, Sc, Ga, Fe, Cr, Al) compounds are taken into account [69–71], as shown in [29]; anyway, the predicted boundary t value based on

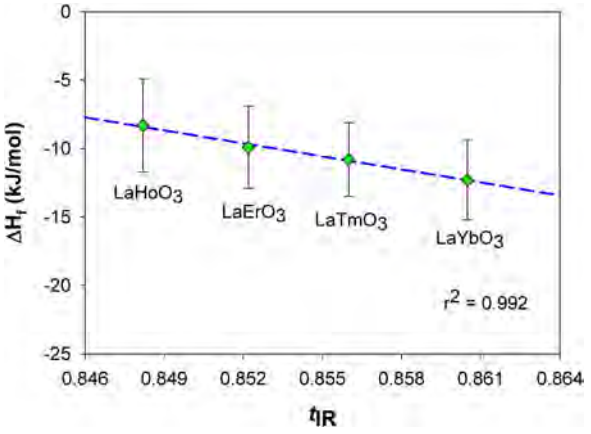

Fig. 5. Formation enthalpies at room temperature of some interlanthanide perovskites as a function of t_{IR}. The r^2 value of the regression line is reported too; data are taken from Ref. [29].

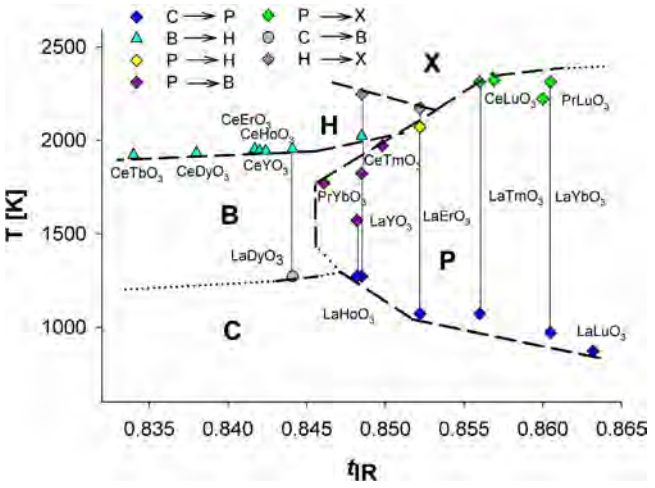

Fig. 6. Stability range of interlanthanide perovskites ABO_3 as a function of t_{IR}. In case of unavailability of the A ionic radius, t_{IR} was calculated from t_{BV} through Eq. (5). Letters identify the phases present: P perovskite; C cubic; B monoclinic; H high temperature hexagonal; X high temperature cubic.

formation enthalpy data results to be lower than experimentally observed.

In Fig. 6 data of transition temperatures of equimolar interlanthanide mixed oxides are represented as a function of t_{IR}. It can be observed that the perovskitic phase (P) is squeezed between other structural forms typical of rare earths sesquioxides: the cubic C, the monoclinic B, or one of the high temperature forms (H: hexagonal, X: cubic [72]). In particular, as can be observed in Fig. 6, interlanthanide perovskites form by thermal decomposition of the mixed oxide in the C form. The latter is characterized by a cubic cell with cations located in two different positions, namely in 24*d* (x, 0, ¼) and 8*a* (0, 0, 0), at the centre of two different distorted octahedra. Therefore, the C → P transition occurs with a change from CN 6 to CN 6/8, *i.e.* with an average coordination number increase, as expected with increasing temperature. At high temperature, perovskites decompose into a solid solution adopting the B, H or X form, depending on the *t* value. As the H and X form are stable only at high temperature, not all their structural details are known, except that they are hexagonal and cubic, respectively, and that both are formed of distorted octahedra [73]. The B form, on the contrary, is the monoclinic structure typical of several rare earth sesquioxides, and it is characterized by the presence of three cationic positions located in 4*i* (*x*, 0, *z*); in mixed oxides belonging to the B form (for example in the La_2O_3-Y_2O_3 system [63,74]), a random distribution of both cations over all the 4*i* sites can be argued by considering the closeness of all the cation-oxygen interatomic distances. Within the perovskitic cell, on the contrary, atoms occupy well defined positions that exclude the possibility of random distribution, due to the aforementioned dimensional constraints; in this respect, the perovskitic phase appears as a highly ordered phase if compared to all other structural forms of rare earth sesquioxides. Therefore, at a certain temperature the P → B transition results to be favoured by the entropic contribution to the Gibbs free energy, due to the substantial disorder increase associated to the atomic rearrangement. Outside the perovskitic stability field, Fig. 6 suggests that with increasing temperature phases follow the sequence C → B → H → X.

Pseudobinary phase diagrams involving interlanthanide perovskites have been studied over the whole compositional range and a large temperature span for La_2O_3-Y_2O_3, La_2O_3-Ho_2O_3, La_2O_3-Er_2O_3, La_2O_3-Tm_2O_3, La_2O_3-Yb_2O_3, La_2O_3-Lu_2O_3 [62,64], while Ce- and Pr-containing mixed oxides have been investigated only at given compositions, such as for example the equimolar one [65]. According to all the pseudobinary phase diagrams shown in the literature, interlanthanide perovskites form through an eutectoidic reaction, irrespective of the identity of the high temperature phase.

The perovskitic phase assumes a nearly-stoichiometric character at low temperature, while with increasing temperature a limited solubility of the smaller oxide within the bigger one is observed, suggesting that, despite the size constraints typical of the phase, a certain substitution of the bigger by the smaller ion is possible. While in La_2O_3-Y_2O_3 the perovskite is reported as essentially stoichiometric, in La_2O_3-Er_2O_3, for example, at 1823 K it extends from $La_{1.02}Er_{0.98}O_3$ to $La_{0.96}Er_{1.04}O_3$ [66]; in the La_2O_3-Yb_2O_3 system, the perovskitic phase reaches the maximum extent of the solid solution at around 2173 K, where it ranges from $La_{1.1}Yb_{0.9}O_3$ to $La_{0.7}Yb_{1.3}O_3$ [62]. A narrow solubility range can be observed also in the Pr_2O_3-Lu_2O_3 pseudobinary syatem at 1673 K (from $Pr_{1.06}Lu_{0.94}O_3$ to $Pr_{0.98}Lu_{1.02}O_3$) [66]. Even for La_2O_3-Tm_2O_3 the compositional extent of the perovskite is remarkably more extended than for La_2O_3-Er_2O_3 [64]. The described evidence indicates that a relationship exists between the size of the smaller cation and the perovskitic solubility range, and suggests that in the La_2O_3-Lu_2O_3 system the perovskitic solubility range should be even larger; nevertheless, experimental data are not available in the literature.

Studies about some pseudoternary systems involving interlanthanide perovskites can be found too: in Ref. [66], for example, ternary sections at 1673 K are reported for the systems Pr_2O_3-Lu_2O_3-Eu_2O_3 and La_2O_3-Y_2O_3-Er_2O_3. In the latter, due to the similarity of Er^{3+} and Y^{3+} radii ($r_{Er3+,CN6}$ = 0.890 Å, $r_{Y3+,CN6}$ = 0.900 Å), a complete solubility between $LaYO_3$ and $LaErO_3$ can be observed, and the maximum solubility range between larger and smaller cations is reached at Er:Y = 1:1, where the perovskitic range spans from $La_{0.47}(Y_{0.265}Er_{0.265})O_3$ to $La_{0.54}(Y_{0.23}Er_{0.23})O_3$. In the Pr_2O_3-Lu_2O_3-Eu_2O_3 system, on the contrary, the $PrLuO_3$ perovskitic range extends only up to 9% Eu.

2.4. Chemical stability

Interlanthanide perovskites are generally reported to be chemically stable against oxygen and carbon dioxide [22]; this property, coupled to the good protonic conduction of some of them when properly doped, makes them interesting candidates to be used in solid oxide fuel cells, as will be discussed later. Nevertheless, Ce- based compounds, due to the presence of Ce^{3+}, undergo in air at relatively low temperatures (443–473 K) the oxidation reaction $CeREO_3 + {}^1\!/\!_4O_2 \rightarrow CeO_2 + {}^1\!/\!_2RE_2O_3$, where RE≡Tm, Yb, Lu. The so obtained products can be characterized by x-ray diffrac-

tion: they consist of fluorite-type CeO_2 and C-type RE_2O_3 [65]. It is noteworthy that the value of the RE_2O_3 lattice parameters experimentally observed from the analysis of the oxidation products, result to be in each case higher than expected. For RE≡Tm, Yb and Lu, a = 10.699 Å, a = 10.678 Å, and a = 10.434 Å, respectively, while the reported values are a_{Tm2O3} = 10.4908 Å [75], a_{Yb2O3} = 10.440(2) Å [76], and a_{Lu2O3} = 10.355 Å [77]. This evidence points to the possible dissolution of a certain amount of Ce^{4+} into the RE_2O_3 lattice, or alternatively to the formation of CeO_2 microdomains, as already observed in the CeO_2-Gd_2O_3 and CeO_2-Sm_2O_3 systems [78,79]; this hypothesis is suggested by the fact that the Ce^{4+} ionic radius (0.97 Å, CN 8) is significantly larger than the ones of Tm^{3+} (0.880 Å, CN 6), Yb^{3+} (0.868 Å, CN 6) and Lu^{3+} (0.861 Å, CN 6).

$PrREO_3$ (RE≡Yb, Lu) perovskites, on the contrary, despite the presence of oxidable Pr^{3+}, need a 8-h lasting thermal treatment at 1673 K in oxidizing environment to react almost completely [65].

2.5. Effect of the cooling rate on the extent of the perovskitic field

The so far developed assessement only includes data of samples considered at the thermodynamic equilibrium; nevertheless, it is possible to extend or contract the existence fields of the perovskitic and of neighbouring phases by acting on the cooling rate. Such a study has been conducted on La_2O_3-RE_2O_3 systems (RE≡Y, Nd, Sm, Gd–Yb) by heating samples up to the melting temperature, and subsequently analyzing phases obtained after quenching (cooling rate: 500 K/s) and splat cooling (cooling rate: 10^4 K/s). The obtained results are compared to the ones deriving from samples annealed at 1673 K [67]. It could be observed that an increase of the cooling rate brings to a remarkable enlargement of the B stability field, so that for RE≡Y, Ho, Er, both in quenched and splat-cooled specimens, the perovskitic compounds do not appear at all. Interestingly, a further effect of a high cooling rate on the systems where the perovskite appears is an increased solubility of RE (RE≡Tm, Yb) within this phase, so that in splat-cooled samples, the La/Yb perovskite extends from $LaYbO_3$ to $La_{0.6}Yb_{1.4}O_3$, *i.e.* over compositions where the binary field (P + C) is expected in equilibrium conditions. The latter evidence can be attributed to a higher formation rate of the perovskite with respect to the C phase.

3. Synthetic methods

Interlanthanide perovskites can be obtained in polycrystalline (powder) and monocrystalline form, and also as thin films; several synthetic paths have been developed with the aim to shorten the processing time, to decrease the treatment temperature, or to extend the stability field of the phase by operating in non-equilibrium conditions. In the following two paragraphs, an overview of the synthetic methods proposed in the literature is provided.

3.1. Polycrystalline samples

Essentially three synthetic methods are proposed in the literature for the preparation of polycrystalline interlanthanide perovskites: (a) solid state reaction of a mixture of oxides or hydroxides; (b) coprecipitation of mixed hydroxides or oxalates; (c) melting of a mixture of oxides followed by annealing or by quenching. A synopsis of the cited synthetic paths is reported in Table 2.

Generally speaking, methods based on wet chemistry (coprecipitation of mixed oxalates or hydroxides) ensure an optimum homogenization degree and allow to use a lower processing temperature and a shorter time than needed by other techniques. A comparison between solid state and coprecipitation method has been made by Berndt et al. [53], who observed that, even if $CeLuO_3$, $CeTmO_3$, $CeYbO_3$ and $PrLuO_3$ can be prepared by both techniques, the former method needs a remarkably longer reaction time, that increases with increasing the cationic size closeness. In the case of $LaErO_3$, for instance, the annealing of coprecipitated hydroxides at 1523 K for two days is sufficient to obtain the pure perovskitic phase, while by the solid state reaction, even after 8 days, the thermal treatment at 1523 K provides $LaErO_3$ mainly in the C form. Similarly, perovskitic $LaHoO_3$ could not be obtained by the solid state reaction at 1673 K or 1873 K of the slurry prepared by ball milling La_2O_3 and Ho_2O_3 in acetone. By this method the perovskitic phase could be obtained only by substituting Ho^{3+} by at least a 5% at. Yb^{3+} [81]. Finally, the attempt to prepare perovskites by coprecipitation of mixed hydroxides followed by hydrothermal reaction at 483 K for 10 days resulted unsuccessful for all compositions [53].

Procedures involving melting of the oxides mixture are quite energy-consuming, but they provide the possibility to observe different phases for a given composition according to the chosen cooling rate, as described in Section 2.3. In particular, increasing the cooling rate causes the reduction of the temperature range and the expansion of the compositional range of the perovskitic phase.

Finally, it has to be mentioned that, even if sporadically, also combustion synthesis is sometimes reported as a proper way for the synthesis of interlanthanide perovskites [83].

3.2. Single crystals

Single crystals of $LaREO_3$ (RE≡Y, Ho-Lu) can be grown from hydroxide fluxes [28]. A melt of KOH and NaOH can in fact dissolve rare earth oxides, as proven for various lanthanide-based perovskites [84]; on the basis of these results, the crystal growth of the aforementioned interlanthanide perovskites was observed in the temperature range 873–1023 K. $LaLuO_3$, as well as Ce- and Pr-doped $LaLuO_3$ were obtained as single crystals by the Czochralski method [85,86].

3.3. Thin films

The deposition of thin films is documented both for $LaYbO_3$ and $LaLuO_3$, as a prerequisite for the study of these oxides as high-k dielectrics. In particular, $LaYbO_3$ was deposited by reactive sputtering on p-type Si (1 1 1) and on quartz substrates using a La-Yb target [87], as well as by pulsed laser deposition (PLD) using a $LaYbO_3$ ceramic target and a $SrTiO_3$ substrate as a part of the tri-layer film $SrRuO_3$/$LaYbO_3$/$SrRuO_3$ [88]. In addition to PLD [89,90], $LaLuO_3$ thin films were also obtained by atomic layer deposition (ALD) [91] and by metal-organic chemical vapor deposition (MOCVD) [92].

4. Properties

In this section the main physical properties of interlanthanide perovskites are described and discussed, namely the optical and magnetic ones, as well as protonic conduction and the high dielectric constant.

4.1. Optical properties

Optical properties of interlanthanide perovskites generally consist in the absorption of radiation in the near-infrared part of the spectrum by the luminescent ion (the activator) present within the structure, and in its re-emission at higher or lower (upconversion) wavelength *via* a combination of different phenomena, such as ground and excited state absorption, and non-radiative relaxation (heat emission). In some cases, the presence of a further luminescent ion, acting as a sensitizer, enhances the emission intensity of the activator by transferring energy to the latter from one of its excited energy levels. Responsible for this phenomenon

Table 2
Synopsis of synthetic methods proposed in the literature for the obtainment of polycrystalline interlanthanide perovskites.

Method	Procedure	Reference
Solid state reaction	Thermal treatment on pellets of stoichiometric mixtures of oxides. Treatment temperature: 1323 K ($LaHoO_3$); 1723 K ($LaREO_3$, RE≡Er-Yb); duration: 36 h.	[29]
	Thermal treatment on stoichiometric mixtures of oxides. Treatment temperature: 1523–1823 K ($LaHoO_3$, $CeLuO_3$, $CeYbO_3$, $CeTmO_3$, $PrLuO_3$, $PrYbO_3$, $NdLuO_3$).	[53]
	Thermal treatment on pellets of stoichiometric mixtures of separately precipitated hydroxides. Treatment temperature: 1523 K ($LaHoO_3$, $CeLuO_3$, $CeYbO_3$, $CeTmO_3$, $PrLuO_3$, $PrYbO_3$, $NdLuO_3$).	[53]
	Thermal treatment on pellets of stoichiometric mixtures of mixed oxides obtained by ball milling in acetone. Treatment temperature: 1573 K and 1673 K; duration: 15 h ($LaYbO_3$).	[80]
	Thermal treatment on pellets of stoichiometric mixtures of mixed oxides obtained by ball milling in ethanol. Treatment temperature: 1673 K and 1873 K in air; duration: 10 h [$LaYO_3$, $LaErO_3$, $LaYbO_3$, $La(Ho,Yb)O_3$].	[81]
	High-pressure (29 kbar) thermal treatment of stoichiometric mixtures of oxides ($LaREO_3$, RE≡Y, Ho, Er, Yb, Lu).	[82]
Coprecipitation	Coprecipitation of mixed oxalates followed by thermal treatment in air at 873–2073 K ($LaREO_3$, RE≡Ho-Lu).	[23]
	Coprecipitation of mixed hydroxides followed by thermal treatment at 1523 K ($LaHoO_3$, $CeLuO_3$, $CeYbO_3$, $CeTmO_3$, $PrLuO_3$, $PrYbO_3$, $NdLuO_3$).	[53]
	Coprecipitation of mixed hydroxides followed by hydrothermal reaction at 483 K for 10 days ($LaHoO_3$, $CeLuO_3$, $CeYbO_3$, $CeTmO_3$, $PrLuO_3$, $PrYbO_3$, $NdLuO_3$).	[53]
	Coprecipitation of mixed hydroxides followed by thermal treatment in air or H_2 at 1273–1773 K ($LaREO_3$, RE≡Ho-Lu; $CeREO_3$, RE≡Tm-Lu; $PrREO_3$, RE≡Yb, Lu).	[18]
Melting	Melting of stoichiometric mixtures of oxides in solar furnace, followed by annealing at 1273, 1473 or 1673 K($LaREO_3$, RE≡Ho-Tm; $PrREO_3$, RE≡Yb, Lu).	[64]
	Melting of stoichiometric mixtures of oxides in solar furnace, followed by annealing at 1673 K for 4 h ($CeREO_3$, RE≡Tm-Lu).	[65]
	Melting of stoichiometric mixtures of oxides in solar furnace, followed by quenching (cooling rate ~500 K/s) ($LaREO_3$, RE≡Y, Ho-Yb)	[67]
	Melting of stoichiometric mixtures of oxides in solar furnace, followed by quenching (cooling rate ~10^4 K/s) ($LaREO_3$, RE≡Y, Ho-Yb)	[67]

are for example many rare earth ions that, if present within a certain matrix, can absorb radiation thanks to the presence of several discrete energy levels in their 4*f* shell. Since the influence of the crystal environment on the 4*f* levels of the luminescent ion is scarce, the phenomenon is mainly dependent on the identity of the luminescent ion itself rather than on the host lattice. The relatively low number of publications on this topic can be attributed to the fact that luminescence of rare-earth doped oxides is a general phenomenon, widely treated in a plenty of works during the last decades with reference to similar compounds, such as aluminates (among them the well known YAG, *i.e.* $Y_3Al_5O_{12}$:Nd^{3+} [93]), rare earth sesquioxides (such as, for example, Lu_2O_3:Eu [94], Gd_2O_3:Er [95] and La_2O_3:Pr^{3+},Yb^{3+} [96]), oxycarbonates $RE_2O_2CO_3$:Eu^{3+} or Tb^{3+} (RE=La, Gd, Y) [97,98] and perovskites (for instance $ATiO_3$:Pr^{3+} with A=Ca, Sr, Ba [99] and $GdAlO_3$:Dy^{3+} [100]). A comprehensive review about rare earth-containing phosphors can be found for example in [101].

Siaï et al. recently studied the emission properties of two interlanthanide perovskites, namely $LaErO_3$ [83] and $LaHoO_3$ [19]. Both systems are ideal, since their optical properties depend only on the presence of the smaller cation, being the 4*f* shell of La^{3+} empty. The emission of $LaErO_3$ and $LaEr_{1-x}Yb_xO_3$ after laser excitation at 800 and 980 nm revealed two different phenomena according to the wavelength of the incident radiation. As depicted in Fig. 7a, the radiation at 800 nm can be absorbed both by Er^{3+} and Yb^{3+}: in Yb-doped samples, in fact, an emission signal at 984 nm can be observed, corresponding to the $^2F_{5/2} \rightarrow {}^2F_{7/2}$ transition of Yb^{3+}; moreover, both in doped and undoped samples, a further signal at 1540 nm can be detected, indicating the occurrence of the $^4I_{13/2} \rightarrow {}^4I_{15/2}$ transition of Er^{3+}. Since the intensity of the latter emission increases with increasing the Yb content, an energy transfer phenomenon from the $^2F_{5/2}$ level of Yb^{3+} to the $^4I_{11/2}$ of Er^{3+}, followed by a non radiative transition to $^4I_{13/2}$, was hypothesized. Thus, this result revealed the role of sensitizer played by Yb^{3+} within the $LaErO_3$ matrix.

The excitation at 980 nm, on the contrary, gives rise to a substantially different phenomenon, as schematized in Fig. 7b. The radiation is in fact absorbed by both ions, as ground state absorption ($^2F_{7/2} \rightarrow {}^2F_{5/2}$ in Yb^{3+} and $^4I_{15/2} \rightarrow {}^4I_{11/2}$ in Er^{3+}), as well as excited state absorption ($^4I_{11/2} \rightarrow {}^4I_{7/2}$ in Er^{3+}); moreover, energy transfer takes place between the $^2F_{5/2}$ level of Yb^{3+} and higher energy levels of Er^{3+}. Thanks to this complex energy redistribution, three emission signals in the visible portion of the spectrum can be observed, meaning that an upconversion phenomenon takes place. In particular, two green emission bands at 527 and 548 nm are visible, due to the $^2H_{11/2} \rightarrow {}^4I_{15/2}$ and the $^4S_{3/2} \rightarrow {}^4I_{15/2}$ transitions, respectively; moreover, a red emission takes place at 660 nm, due to the $^4F_{9/2} \rightarrow {}^4I_{15/2}$ transition. All these transitions take place after a non radiative relaxation from the $^4F_{7/2}$ level. Even in the present case, Yb^{3+} acts as a sensitizer, since all the aforementioned emissions are enhanced in Yb-doped samples.

Emission phenomena associated to the $LaHoO_3$ perovskite under excitation at 488 nm are schematized in Fig. 8a. They essentially consist in three signals at 548, 665 and 754 nm, due to the $^5S_2$, $^5F_4, \rightarrow {}^5I_8$, $^5F_5, \rightarrow {}^5I_8$, and $^5S_2$, $^5F_4, \rightarrow {}^5I_7$ transitions, respectively. The excitation at 750 nm, on the contrary, promotes the emission at 1340 nm, ascribable to the $^5S_2$, $^5F_4, \rightarrow {}^5I_5$ transition (see Fig. 8b).

Based on the described results, both $LaEr_{1-x}Yb_xO_3$ and $LaHoO_3$ can be classified as phosphors. The high emission intensity of $LaHoO_3$ in the infrared range suggests the employment of this material as a solid state laser; similarly, due to the intense emission at 527 and 548 nm, $LaEr_{1-x}Yb_xO_3$ is a promising upconversion green laser.

Absorption spectra of Ce^{3+} (characterized by the presence of one *f* electron) were studied some decades ago by J. Coutures and J. P. Coutures [65] on Ce-based perovskitic and non perovskitic $CeREO_3$

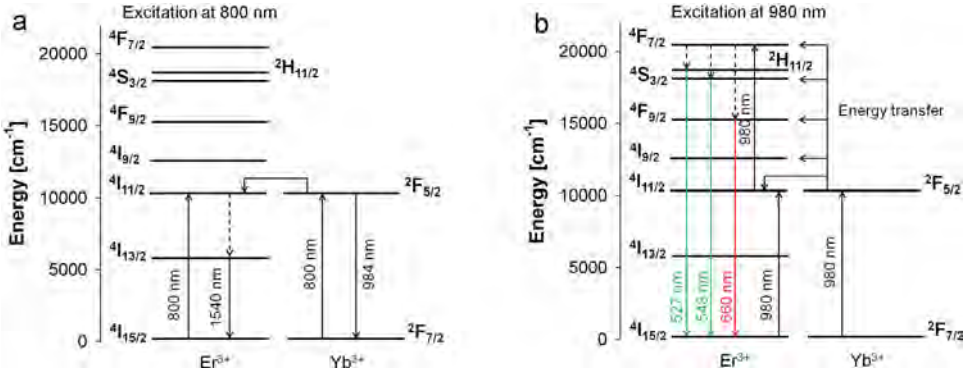

Fig. 7. Energy level diagram of Er^{3+} and Yb^{3+} showing emission paths after excitation at a) 800 nm and b) 980 nm (redrawn from Ref. [83]).

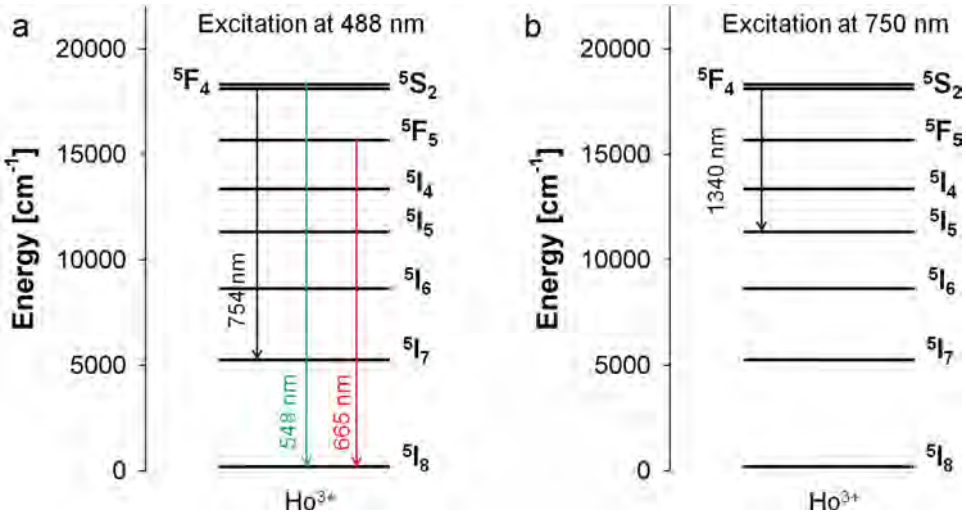

Fig. 8. Energy level diagram of Ho^{3+} showing emission paths after excitation at a) 488 nm and b) 750 nm (after Ref. [19]).

oxides (RE≡La-Nd: hexagonal A structure; RE≡Eu-Tm, monoclinic B structure; RE ≡Tm-Lu: perovskitic structure). Even if limited to the high energy range (19000–23000 cm^{-1}), thus allowing to observe the $^2F_{5/2} \rightarrow 5d$ transition and not the $^2F_{5/2} \rightarrow {}^2F_{7/2}$ transition, the investigation is particularly interesting because it highlights the role of the crystalline environment in tuning the value of the absorption energy. While in fact *f* levels are scarcely influenced by the crystal surroundings, when dealing with *d* bands the effect of the matrix can not be neglected. A slightly decreasing trend of the absorption energy is observed with decreasing the size of the smaller cation, but at the monoclinic/perovskitic boundary (*i.e.* between monoclinic and perovskitic $CeTmO_3$), a remarkable gap ($\Delta E \sim 1600\ cm^{-1}$) appears towards lower energy values for the perovskitic structure. This evidence is attributed to the role of the different structures of mixed oxides, and in particular to the Ce^{3+} coordination number, that at the monoclinic/perovskitic boundary changes from 6/7 to 12. This variation of the coordination number induces an expansion of the Ce^{3+} ion (from 1.07 Å to 1.34 Å), that reduces the energy gap between ground and excited state.

4.2. Magnetic properties and specific heat

A complete investigation of magnetism of interlanthanide perovskites was recently performed by this and other research groups [18,23,24]. As a general remark, electrons populating the 4*f* levels are responsible also for the magnetic properties of the studied compounds. Magnetic cooperative phenomena are related to the presence of Kramers' ions, *i.e.* ions possessing an odd number of unpaired electrons; the latter can explain the antiferromagnetism of $LaErO_3$, $LaYbO_3$, $CeYbO_3$ and $PrYbO_3$ (Er^{3+} and Yb^{3+} possess 11 and 13 *f* electrons, respectively).

A general agreement exists in the literature about the antiferromagnetic ordering taking place in perovskitic $LaErO_3$ below 2.4 K: it was studied by neutron powder diffraction in the Sixties of last century by Moreau et al. [102,103], and more recently by magnetization, specific heat [18,104] and again neutron powder diffraction [24]. An analogous cooperative behaviour was observed also in Yb-containing perovskites ($LaYbO_3$, $CeYbO_3$ and $PrYbO_3$), with comparable Néel temperatures of 2.7 K. It is noteworthy that Néel temperatures of the studied compounds are always very low, as expected for cooperative phenomena deriving from superexchange, that takes place among rare earth ions connected through very weak interatomic interactions. Specific heat measurements performed on $LaErO_3$ and $LaYbO_3$ show the presence of a λ-type curve in correspondence of the Néel temperature; the subtraction of the electronic and lattice contribution, performed by subtracting the specific heat of diamagnetic $LaLuO_3$ from the curves of antiferromagnetic perovskites, allows to entirely attribute the λ anomaly to the magnetic contribution, as shown in [18]. All the other perovskites were found to be paramagnetic down to 1.8 K, except $LaLuO_3$, which is diamagnetic. Magnetic properties deriving from the presence of rare earths within ionic or covalent compounds result from the competition between spin-orbit coupling and crystal field, with the latter that lifts the degeneracy of the 4*f* levels. The crystal field effect can be observed in interlanthanide perovskites in the trend of the inverse magnetic susceptibility (χ^{-1})

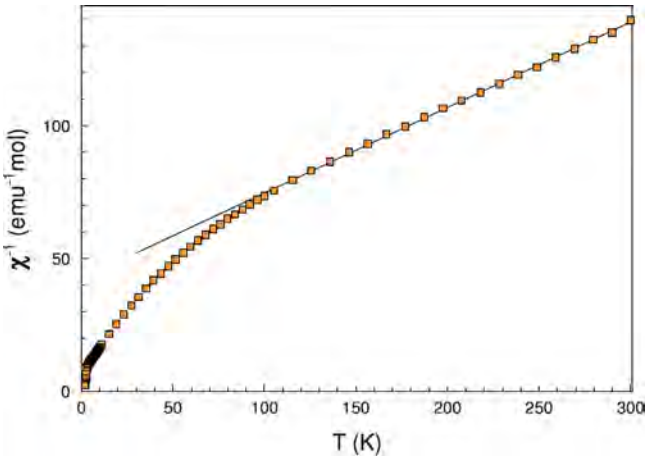

Fig. 9. Trend of the $LaYbO_3$ inverse susceptibility as a function of temperature. (Taken from Ref. [23]; ©IOP Publishing. Reproduced with permission. All rights reserved).

at low temperature. χ^{-1} vs. T of $LaYbO_3$ is for example reported in Fig. 9: as indicated by the regression line interpolating high temperature data, the curve can be fitted at T > ~100 K by the Curie-Weiss law

$$\chi = \frac{C}{T-\theta} \tag{6}$$

where C is the Curie constant

$$C = \frac{N_A \mu_{eff}^2}{3k} \tag{7}$$

θ the Weiss temperature, N_A the Avogadro number, μ_{eff} the effective magnetic moment, and k the Boltzmann constant. At low temperature, on the contrary, experimental data deviate from the Curie-Weiss curve; this behaviour can be explained taking into account the splitting of the $^2F_{7/2}$ Yb^{3+} ground state operated by the crystal field, that becomes evident at temperatures that do not allow higher levels to be populated. With further decreasing temperature, the exchange interactions between Yb^{3+} ions start prevailing, and below 2.7 K the compound undergoes an antiferromagnetic ordering. The attribution of the deviation from the Curie-Weiss curve to the crystal field effect is confirmed by susceptibility measurements performed on paramagnetic $LaHoO_3$, that show a similar behaviour at temperatures lower than 20 K: in this case, in fact, the evidence can be entirely ascribed to the crystal field, due to the absence of magnetic ordering.

Magnetization measurements performed on $LaYbO_3$ at 1.8 K highlight the existence of a hysteresis loop [23,18], pointing at the presence of a ferromagnetic contribution to the magnetic ordering; a similar evidence was found also in $CeYbO_3$ and $PrYbO_3$, but not in $LaErO_3$ [18]. This point is corroborated by neutron powder diffraction data collected on $LaYbO_3$ at 1.5 K [23], that show an increase in the scattered intensity of two peaks, compatible with a weak ferromagnetic component. In Fig. 10 the crystal structure associated to the scheme of spin ordering is shown for both $LaYbO_3$ and $LaErO_3$, as deriving from the neutron diffraction analysis: as hypothesized by Ito et al. [18], the observed ferromagnetic component of $LaYbO_3$ is related to the canting of Yb^{3+} spins, while no net resulting moment appears in $LaErO_3$. In $LaYbO_3$, in fact, magnetic moments lie in the equatorial plane of the YbO_6 octahedra, while in $LaErO_3$ they point to the centre of an octahedron edge, as observable in Fig. 11 (taken from Ref. [24]).

4.3. Protonic conduction

Protonic conduction is a well known and widely investigated phenomenon in many oxides, and in particular in perovskites [105,106]: $SrCeO_3$- [107], $BaCeO_3$- [108] and $CaZrO_3$- [109] based perovskites, as well as the more complex oxide $Ba_3Ca_{1.18}Nb_{1.82}O_{9-\delta}$ [110] for example, are among the most studied and used systems showing this property.

Protonic conduction has been observed in several La-containing interlanthanide perovskites with La partially substituted by a bivalent ion, such as Ca^{2+} or Sr^{2+}. In particular, the phenomenon is well established in $LaYO_3$- [20,111,112], $LaErO_3$- [30], $LaYbO_3$- [20–22,113] and $LaLuO_3$- [114,115] based perovskites; it takes place at high temperature in wet atmosphere, as a consequence of the ability of the structure to trap and dissociate water. With respect to the cerates and zirconates, interlanthanide perovskites-based protonic conductors are characterized by a higher stability to carbon dioxide [22], which makes them interesting candidates for the employment in SOFC's.

The mechanism of proton transport in such compounds has been nicely depicted on the basis of atomistic modelling [116,117], and experimental data satisfactorily confirm theoretical predictions. The presence of protons within the perovskitic structure is strictly related to the formation of oxygen vacancies, that occurs when La^{3+} is partially substituted by a bivalent ion (such as an alkaline earth, Ae^{2+}), according to the following equation:

$$La_{La} + AeO \rightarrow Ae'_{La} + \frac{1}{2}V_{\ddot{O}} + \frac{1}{2}La_2O_3 \tag{8}$$

In agreement with the ability to dissociate water shown by several perovskites with oxygen vacancies, protons enter the

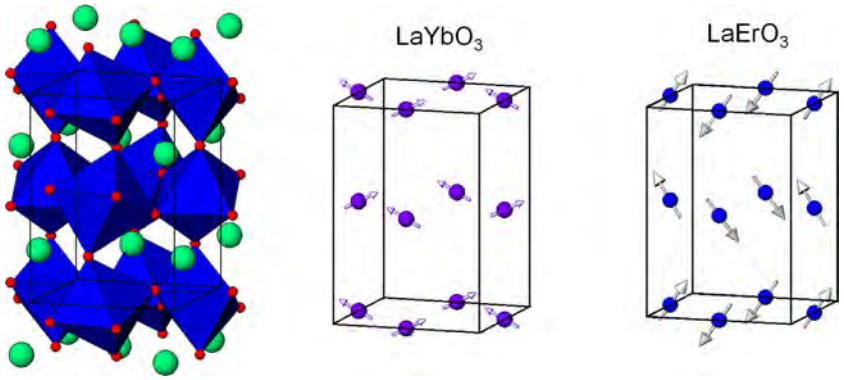

Fig. 10. Crystal structure and associated scheme of the orientation of magnetic moments in $LaYbO_3$ and $LaErO_3$. (Taken from Refs. [23] and [24]; ©IOP Publishing. Reproduced with permission. All rights reserved).

oxygen-deficient structure *via* filling oxygen vacancies by hydroxyl ions deriving from water, according to the following equation:

$$H_2O_{(g)} + V_{\ddot{O}} + O_O^x \rightarrow 2OH^{\cdot} \quad (9)$$

The reaction of water incorporation results to be exothermic, meaning that the proton uptake is favoured at low temperatures. This prediction agrees well with the classification of these oxides as proton/oxygen/*p*-type electronic mixed conductors, according to temperature and oxygen partial pressure: in water vapour atmosphere, for example, $(La_{0.9}Sr_{0.1})MO_{3-\delta}$ with M≡Lu, Sc or In is a predominantly proton conductor at T < 873 K, and a *p*-type electronic conductor at higher temperature [114]. In the described reaction scheme, protons are bound to a neighbouring oxygen atom through hydrogen bonds, and located in interstitial positions; deuterium/hydrogen isotope effect measurements, moreover, show that proton transport takes place essentially thanks to proton hopping, rather than to hydroxyl migration [118]. This mechanism implies the switch of the proton between two neighbouring oxygen atoms *via* the passage through a barrier state; theoretical calculations show that the energy barrier increases with increasing the distance between the aforementioned oxygen atoms [117].

The protonic conduction in the studied oxides reveals to depend on many interconnected parameters, dealing both with the equilibrium constant of proton incorporation and with proton mobility. $LaErO_3$-based protonic conductors, for instance, show a very high reaction constant for water incorporation, but a lower protonic conductivity with respect to $LaYO_3$-based conductors, meaning that the proton mobility is much higher in the latter [112].

Two main structural parameters play a role in tuning proton conduction, both related to the identity of the bivalent ion and of the B ion. According to theoretical calculations [117], the energy associated to the dissolution of different alkaline-earth ions into La-based perovskites shows a minimum in correspondence of Ca^{2+} and Sr^{2+}, *i.e.* the ions that present the minimum size difference with respect to La^{3+}. This result indicates that the cited ions are expected to promote the maximum proton uptake; Ca^{2+} and Sr^{2+} are therefore the most used doping ions in experimental studies. Nevertheless, it has to be pointed out that the amount of incorporated protons generally does not correspond to the concentration of the doping ion; this is particularly evident in Sr-doped $LaYbO_3$ and $LaYO_3$ [20,112], and it has been attributed to a particularly high stability of some oxygen vacancies, as well as to the formation of stable associations of vacancies and doping ions.

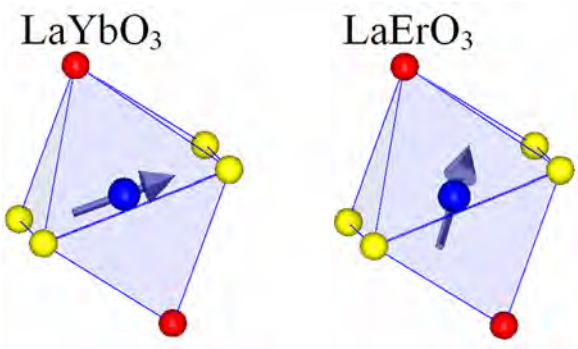

Fig. 11. Orientation of magnetic moments within ErO_6 and YbO_6 octahedra. Blue spheres: Er/Yb; red spheres: axial oxygen; yellow spheres: equatorial oxygen. (Taken from Ref. [24]; ©IOP Publishing. Reproduced with permission. All rights reserved). (For interpretation of the references to colour in this figure legend, the reader is referred to the web version of this article.)

The issue related to the effect of the M ionic size has been treated for the systems $(La_{0.9}Sr_{0.1})MO_{3-\delta}$ with M≡Sc, In and Lu [114,115], where the protonic conduction increases with decreasing the size of M, *i.e.* with decreasing the perovskitic distortion. A correlation between O–O distances within the perovskite and proton mobility has been highlighted for Y-doped cerates [119], and put in relation with the dimensionality of the proton exchange, that changes from one- to three- dimensional with approaching the perovskitic ideality. On this basis, a crystallographic study was performed at 873 K on $(La_{0.9}Sr_{0.1})MO_{3-\delta}$ (M≡Sc, In and Lu) by taking into account the experimental O–O distances within the MO_6 octahedron (*i.e.* the ones along the octahedra edges) and between neighbouring octahedra. On going from Lu ($r_{Lu3+,CN6}$ = 0.861 Å) to Sc ($r_{Sc3+,CN6}$ = 0.745 Å) at the M site, the distortion of octahedra decreases, and consequently oxygen atoms belonging to different octahedra progressively move away; therefore, the O–O distance within octahedra becomes shorter than the one between octahedra, and the three- dimensional pathway shown in Fig. 12a) is energetically favoured with respect to the one-dimensional one highlighted in Fig. 12b). The occupation of the B site by larger atoms, on the contrary, causes the intra- and inter-octahedral O–O distances to become comparable, so that when the B site is occupied by Lu, the one-dimensional pathway is favored, with a consequent reduction in the value of protonic conductivity. The depicted three dimensional protonic exchange is the one occurring in the

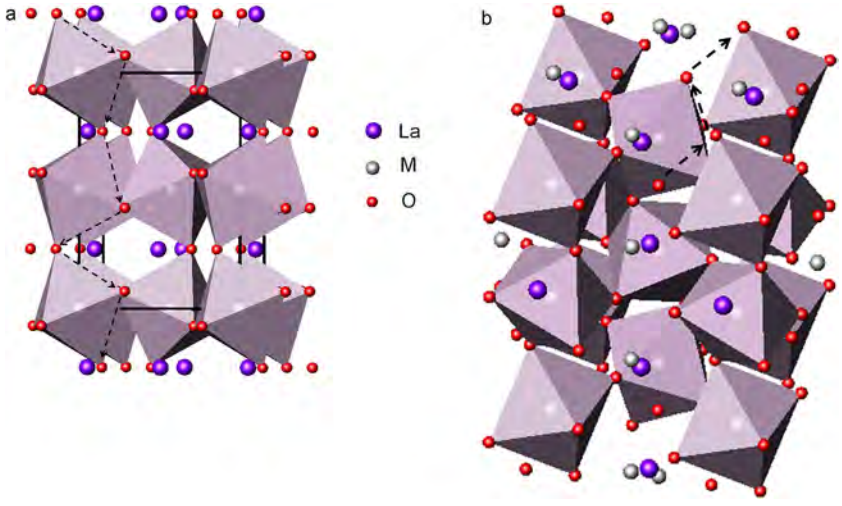

Fig. 12. a) Three-dimensional and b) one-dimensional possible pathways of proton conduction. Arrows indicate the direction of hopping and highlight the oxygen atom bound to the proton.

most performing $A^{2+}B^{4+}O_3$ perovskitic protonic conductors, such as $Ba(Ce_{0.9}Y_{0.1})O_{3-\delta}$ and $Sr(Ce_{0.9}Y_{0.1})O_{3-\delta}$.

Also the catalytic activity of some acceptor-doped interlanthanide perovskites seems to be related to the mechanism of proton uptake that occurs in these compounds [112]. $La_{0.8}Sr_{0.2}YO_{3-\delta}$, for example, is able to catalyze the oxidation of CH_4, but it is a poor catalyst for CO [10]; other perovskites, such as $(La_{0.9}Sr_{0.1})MO_{3-\delta}$ with M≡Co, Cr, Fe or Mn, on the contrary, catalyze even the latter reaction, but are less efficient than $La_{0.8}Sr_{0.2}YO_{3-\delta}$ towards the former. While $La_{0.8}Sr_{0.2}YO_{3-\delta}$ below 773 K is a good protonic conductor and a poor *p*-type conductor, the other perovskites are good *p*-type conductors. The catalytic oxidation of CH_4 seem thus to be related to the absorption of H_2 from CH_4, *i.e.* to an appreciable proton uptake; this hypothesis is confirmed by the poor catalytic efficiency of $La_{0.8}Sr_{0.2}YO_{3-\delta}$ towards the oxidation of CO.

4.4. Dielectric properties

Currently, the breakthrough application of some interlanthanide perovskites is related to their high dielectric constant, that make them ideal candidates to substitute SiO_2 as a gate oxide in metal-oxide-semiconductor field-effect transistors (MOSFETs). The rush towards miniaturization of microelectronic devices imposes a progressive reduction of the oxide layer thickness, in order to increase the capacitance; nevertheless, a SiO_2 thickness lower than 2 nm induces the appearance of significant leakage currents that make this oxide unsuitable for further downscaling. In this framework, some interlanthanide perovskites, such as $LaYbO_3$ and $LaLuO_3$, have been theoretically predicted [120], as well as experimentally found [87,88,121], to properly substitute the aforementioned oxide, not only due to their high value of the dielectric constant, but also in terms of compatibility with the Si substrate. Microwave dielectric properties were also studied for $LaYbO_3$ and found to show lower high quality factor and near-zero coefficient of resonant frequency with respect to $LaGaO_3$ and $LaAlO_3$, despite the similar values of dielectric constant [80].

5. Conclusions

The reduced size difference between the two cations and the presence of the deep-lying 4*f* electrons determines the structural and the physical properties of the eleven interlanthanide perovskites; moreover, the ability to dissociate water and to substitute oxygen vacancies with hydroxyl groups, drives the remarkable properties of protonic conduction observed in some acceptor-doped La-based perovskites.

Due to the dimensional constraint, these oxides must adopt a strongly distorted perovskitic structure, that progressively reduces the temperature stability range with decreasing the value of the Goldschmidt *t* factor. For the same reason, interlanthanide perovskites are located at the boundary of the perovskitic field in all the structure maps proposed in the literature.

Both optical and magnetic properties are strictly related to the presence of well separated *f* energy levels; all the phenomena of radiative emission observed in $LaErO_3$ and $LaHoO_3$, for example, can be interpreted on the basis of the associated energy levels scheme. Concerning magnetism, the deviation from the Curie-Weiss behaviour observed at low temperature in perovskites such as $LaYbO_3$, results from the splitting of the ground state operated by the crystal field.

Acknowledgements

Dr. Marcella Pani (University of Genova) is kindly acknowledged for the helpful discussions and the revision of the manuscript. This research did not receive any specific grant from funding agencies in the public, commercial, or not-for-profit sectors.

References

[1] C. Artini, G.A. Costa, M.M. Carnasciali, R. Masini, Comparative study and properties of $RuSr_2Gd_{1.4}Ce_{0.6}Cu_2O_{10-\delta}$ ruthenocuprate samples by different preparation methods, Mater. Sci. Eng. B 177 (2012) 112–116.
[2] Y. Arachi, T. Asai, O. Yamamoto, Y. Takeda, N. Imanishi, Oxygen-deficient perovskite compounds with oxide ion conduction, Solid State Ionics 135 (2000) 757–760.
[3] H. Ullmann, N. Trofimenko, A. Naoumidis, D. Stöver, Ionic/electronic mixed conduction relations in perovskite-type oxides by defect structure, J. Eur. Ceram. Soc. 9 (1999) 791–796.
[4] T. Ishihara, H. Matsuda, Y. Takita, Doped $LaGaO_3$ perovskite type oxide as a new oxide ionic conductor, J. Am. Chem. Soc. 116 (1994) 3801–3803.
[5] H. Iwahara, T. Esaka, H. Uchida, N. Maeda, Proton conduction in sintered oxides and its application to steam electrolysis for hydrogen production, Solid State Ionics 3–4 (1981) 359–363.
[6] Q. Zhang, H. Sun, X. Wang, Y. Zhang, X. Li, Strong photoluminescence and piezoelectricity properties in Pr-doped $Ba(Zr_{0.2}Ti_{0.8})O_3$–$(Ba_{0.7}Ca_{0.3})TiO_3$ ceramics: influence of concentration and microstructure, J. Eur. Ceram. Soc. 34 (2014) 1439–1444.
[7] A.A. Spivakov, Yu.N. Zakharov, N.V. Ter-Oganessian, A.G. Lutokhin, E.M. Panchenko, V.P. Sakhnenko, Interrelation of ferroelectricity and tilting in perovskites using the phase transitions in $PbZr_{1-x}Ti_xO_3$ as an example, Solid State Sci. 40 (2015) 105–110.
[8] A. Martinelli, M. Ferretti, C. Castellano, M.R. Cimberle, C. Ritter, Effect of Cu^{2+} and Ni^{2+} substitution at the Mn site in $(La_{0.63}Ca_{0.37})MnO_3$: a neutron powder diffraction investigation, J. Solid State Chem. 200 (2013) 128–135.
[9] H. Padma Kumar, S. Saravana Kumar, Meenu Venugopal, R. Binila, K.M. Nissamudeen, J.K. Thomas, Sam Solomon, Synthesis, characterization and photoluminescent properties of $BaZr_xNd_{1-}xO_3$ perovskites, J. Alloys Compd. 629 (2015) 173–177.
[10] R. Doshi, C.B. Alcock, N. Gunasekaran, J.J. Carberry, Carbon monoxide and methan oxidation properties of oxide solid solution catalysts, J. Catal. 140 (1993) 557–563.
[11] A. Oleaga, A. Salazar, D. Skrzypek, Critical behaviour of magnetic transitions in $KCoF_3$ and $KNiF_3$ perovskites, J. Alloys Compd. 629 (2015) 178–183.
[12] Jonathan M. Polfus, Reidar Haugsruds, Protons in perovskite nitrides and oxide nitrides: a first principles study of $ThTaN_3$ and $SrTaO_2N$, Solid State Commun. 152 (2012) 1921–1923.
[13] S.H. Porter, Z. Huang, Z. Cheng, M. Avdeev, Z. Chen, S. Dou, P.M. Woodward, Structural and magnetic properties of $RTiNO_2$ (R = Ce, Pr Nd) perovskite nitride oxides, J. Solid State Chem. 226 (2015) 279–285.
[14] R. Martínez-Coronado, J. Sánchez-Benítez, M. Retuerto, M.T. Fernández-Díaz, J.A. Alonso, High-pressure synthesis of $Na_{1-x}Li_xMgH_3$ perovskite hydrides, J. Alloys Compd. 522 (2012) 101–105.
[15] S. Schneider, R. Roth, Perovskite-type compounds in binary rare earth oxide systems, J. Am. Ceram. Soc. 43 (1960) 115.
[16] H. Müller-Buschbaum, C. Teske, Untersuchung des Systems La_2O_3-Yb_2O_3, Z. Anorg. Allg. Chem. 369 (1969) 249–254.
[17] H. Müller-Buschbaum, C. Teske, Zur Kenntnis der Kristallstruktur von $LaYbO_3$, Z. Anorg. Allg. Chem. 369 (1969) 255–264.
[18] K. Ito, K. Tezuka, Y. Hinatsu, Preparation magnetic susceptibility, and specific heat on interlanthanide perovskites ABO_3 (A = La, Nd, B = Dy, Lu), J. Solid State Chem. 157 (2001) 173–179.
[19] A. Siaï, K. Horchani-Naifer, P. Haro-Gonzàlez, M. Férid, Effect of the preparation processes on structural electronic, and optical properties of $LaHoO_3$, Mater. Res. Bull. 76 (2016) 179–186.
[20] Y. Okuyama, T. Kozai, S. Ikeda, M. Matsuka, T. Sakai, H. Matsumoto, Incorporation and conduction of proton in Sr-doped $LaMO_3$ (M = Al, Sc, In, Yb, Y), Electrochim. Acta 125 (2014) 443–449.
[21] Y. Okuyama, T. Kozai, T. Sakai, M. Matsuka, H. Matsumoto, Proton transport properties of $La_{0.9}M_{0.1}YbO_{3-\delta}$ (M = Ba, Sr, Ca, Mg), Electrochim. Acta 95 (2013) 54–59.
[22] T. Sakai, K. Isa, M. Matsuka, T. Kozai, Y. Okuyama, T. Ishihara, H. Matsumoto, Electrochemical hydrogen pumps using Ba doped $LaYbO_3$ type proton conducting electrolyte, Int. J. Hydrogen Energy 38 (2013) 6842–6847.
[23] A. Martinelli, R. Masini, C. Artini, G.A. Costa, L. Keller, DC magnetic susceptibility and neutron powder diffraction analysis of the perovskite-type compounds $LaYbO_3$ and $LaHoO_3$, J. Phys.: Condens. Matter 25 (2013) 1–7, 426005.
[24] A. Martinelli, C. Artini, L. Keller, New insights into the magnetic properties of $LaErO_3$, $(La_{0.5}Er_{0.5})_2O_3$ and $(La_{0.5}Dy_{0.5})_2O_3$ oxides, J. Phys.: Condens. Matter 28 (2016) 1–9, 066003.
[25] C. Artini, G.A. Costa, M.M. Carnasciali, R. Masini, Stability fields and structural properties of intra rare earths perovskites, J. Alloys Compd. 494 (2010) 336–339.
[26] C. Artini, G.A. Costa, R. Masini, Study of the formation temperature of mixed $LaREO_3$ (REDy, Ho Er, Tm, Yb, Lu) and $NdGdO_3$ oxides, J. Therm. Anal. Calorim. 103 (2011) 17–21.
[27] C. Artini, M. Pani, A. Lausi, G.A. Costa, Stability of interlanthanide perovskites ABO_3 (ALa-Pr; BY, Ho-Lu), J. Phys. Chem. Solids 91 (2016) 93–100.

[28] M. Bharathy, A.H. Fox, S.J. Mugavero, H.C. zurLoye, Crystal growth of inter-lanthanide $LaLn'O_3$ (Ln′=Y, Ho–Lu) perovskites from hydroxide fluxes, Solid State Sci. 11 (2009) 651–654.
[29] J. Qi, X. Guo, A. Mielewczyk-Gryn, A. Navrotsky, Formation enthalpies of $LaLn'O_3$ (Ln = Ho, Er, Tm and Yb) interlanthanide perovskites, J. Solid State Chem. 227 (2015) 150–154.
[30] Y. Larring, T. Norby, Protons in $LaErO_3$, Solid State Ionics 70–71 (1994) 305–310.
[31] R. Pelosato, G. Cordaro, D. Stucchi, C. Cristiani, G. Dotelli, Cobalt based layered perovskites as cathode material for intermediate temperature Solid Oxide Fuel Cells: a brief review, J. Power Sources 298 (2015) 46–67.
[32] A. Chroneos, R.V. Vovk, I.L. Goulatis, L.I. Goulatis, Oxygen transport in perovskite and related oxides: a brief review, J. Alloys Compd. 494 (2010) 190–195.
[33] J.L. Routbort, K.C. Goretta, R.E. Cook, J. Wolfenstine, Deformation of perovskite electronic ceramics–a review, Solid State Ionics 129 (2000) 53–62.
[34] S. Vasala, M. Karppinen, $A_2B'B''O_6$ perovskites: a review, Prog. Solid State Chem. 43 (2015) 1–36.
[35] C.P. Khattak, F.F.Y. Wang, Perovskites and garnets, in: K.A. Gschneidner Jr., L. Eyring (Eds.), Handbook on the Physics and Chemistry of Rare Earths, vol. 3, North Holland Publishing Company, Amsterdam, 1979, pp. 525–607.
[36] P.M. Woodward, Octahedral tilting in perovskites. I. Geometrical considerations, Acta Cryst. B 53 (1997) 32–43.
[37] P.M. Woodward, Octahedral tilting in perovskites. II. Structure stabilizing forces, Acta Cryst. B 53 (1997) 44–66.
[38] V.B. Shirokov, V.I. Torgashev, Tilting structures in perovskites, Crystallogr. Rep. 49 (2004) 20–28.
[39] A.M. Glazer, The classification of tilted octahedra in perovskites, Acta Cryst. B 28 (1972) 3384–3392.
[40] K.S. Aleksandrov, Successive structural phase transitions in perovskites. 1. Symmetry of distorted phases, Kristallografiya 21 (1976) 249–255.
[41] H. Müller-Buschbaum, C. Teske, Untersuchung am System La_2O_3-Yb_2O_3 und über die Kristallstruktur von Yb_2O_3, Inorg. Nucl. Chem. Lett. 4 (1968) 151–152.
[42] R.L. Moreira, A. Feteira, A. Dias, Raman and infrared spectroscopic investigations on the crystal structure and phonon modes of $LaYbO_3$ ceramics, J. Phys.: Condens. Matter 17 (2005) 2775–2781.
[43] V.M. Goldschmidt, Die Gesetze der Kristallochemie, Naturwissenschaften 14 (1926) 477–485.
[44] R.D. Shannon, Revised effective ionic radii and systematic studies of interatomic distances in halides and chalcogenides, Acta Cryst. A 32 (1976) 751–767.
[45] L.H. Ahrens, Geochim. Cosmochim. Acta 2 (1952) 155–169.
[46] S.J. Schneider, R.S. Roth, Phase equilibria in systems involving the rare-earth oxides. Part II. Solid state reactions in trivalent rare-earth oxide systems, J. Res. Nat. Bur. Stand. A 64 (1960) 317–332.
[47] C.A. Randall, A.S. Bhalla, T.R. Shrout, L.E. Cross, Classification and consequences of complex lead perovskite ferroelectrics with regard to B-site cation order, J. Mater. Res. 5 (1990) 829–834.
[48] M.W. Lufaso, P.M. Woodward, Prediction of the crystal structures of perovskites using the software program SPuDS, Acta Cryst. B 57 (2001) 725–738.
[49] I.D. Brown, D. Altermatt, Bond-valence parameters obtained from a systematic analysis of the Inorganic Crystal Structure Database, Acta Cryst. B 41 (1985) 244–247.
[50] http://www.iucr.org/...data/assets/file/0015/120525/bvparm2013.cif.
[51] H. Zhang, N. Li, K. Li, D. Xue, Structural stability and formability of ABO_3-type perovskite compounds, Acta Cryst. B 63 (2007) 812–818.
[52] D.J.M. Bevan, E. Summerville, Mixed rare earth oxides, in: K.A. Gschneidner, L. Eyring (Eds.), Handbook on the Physics and Chemistry of Rare Earths, vol. 3, North Holland Publishing Company, Amsterdam, 1979, pp. 401–524.
[53] U. Berndt, D. Maier, C. Keller, Phasengleichewichte in Interlanthanidenoxid-Systemen, J. Solid State Chem. 13 (1975) 131–135.
[54] E. Mooser, W.B. Pearson, On the crystal chemistry of normal valence compounds, Acta Cryst. 12 (1959) 1015–1022.
[55] J.C. Phillips, J.A. Van Vechten, Spectroscopic analysis of cohesive energies and heats of formation of tetrahedrally coordinated semiconductors, Phys. Rev. B 2 (1970) 2147–2160.
[56] P. Villars, F. Hulliger, Structural-stability domains for single-coordination intermetallic phases, J. Less-Common Met. 132 (1970) 289–315.
[57] R.S. Roth, Classification of perovskite and other ABO_3-type compounds, J. Res. Natl. Bur. Std. 58 (1957) 75–88.
[58] C. Li, K.C.K. Soh, P. Wu, Formability of ABO_3 perovskites, J. Alloys Compd. 372 (2004) 40–48.
[59] D.M. Giaquinta, H.-C. zur Loye, Structural predictions in the ABO_3 phase diagram, Chem. Mater. 6 (1994) 365–372.
[60] I.D. Brown, Bond valences–a simple structural model for inorganic chemistry, Chem. Soc. Rev. 7 (1978) 359–376.
[61] I.D. Brown, The Chemical Bond in Inorganic Chemistry–the Bond Valence Model, Oxford University Press, New York, USA, 2002.
[62] A. Rouanet, J. Coutures, M. Foex, Etude à haute temperature du diagramme d'equilibre du système La_2O_3-Yb_2O_3, J. Solid State Chem. 4 (1972) 219–222.
[63] J. Coutures, M. Foex, Etude à haute temperature du diagramme d'equilibre du système formé par le sesquioxide de lanthane avec le sesquioxide d'yttrium, J. Solid State Chem. 11 (1974) 294–300.
[64] J. Coutures, A. Rouanet, R. Verges, M. Foex, Etude à haute temperature des systèmes par le sesquioxide de lanthane et les sesquioxides de lanthanides. I. Diagrammes de phases (1400 °C < T < T liquide), J. Solid State Chem. 17 (1976) 171–182.
[65] J. Coutures, J.P. Coutures, Etude des solutions solides $CeLnO_3$ et des perovskites $CeLnO_3$ et $PrLnO_3$ (Ln = element lanthanidique), J. Solid State Chem. 19 (1976) 29–33.
[66] U. Berndt, D. Maier, C. Keller, New $A^{III}B^{III}$ O_3 interlanthanide perovskite compounds, J. Solid State Chem. 16 (1976) 189–195.
[67] J. Coutures, F. Sibieude, M. Foex, Etude à haute temperature des systems formés par les sesquioxides de lanthane avec les sesquioxides de lanthanides. II. Influence de la trempe sur la nature des phases obtenues à la temperature ambiante, J. Solid State Chem. 17 (1976) 377–384.
[68] W. Su, D. Wu, X. Ma, Q. Zhengnan, Y. Wang, X. Li, J. Zhou, D. Wang, An investigation using high-pressure synthesis of double-rare-earth oxides of ABO_3-composition, Physica B+C 139–140 (1986) 658–660.
[69] J. Cheng, A. Navrotsky, Enthalpies of formation of $LaBO_3$ perovskites (B = Al, Ga Sc, In), J. Mater. Res. 18 (2003) 2501–2508.
[70] J. Cheng, A. Navrotsky, X.-D. Zhou, H.U. Anderson, Enthalpies of formation of $LaMO_3$ perovskites (M = Cr, Fe Co, Ni), J. Mater. Res. 20 (2005) 191–200.
[71] Y. Kanke, A. Navrotsky, A calorimetric study of the lanthanide aluminum oxides and the lanthanide gallium oxides: stability of the perovskites and the garnets, J. Solid State Chem. 141 (1998) 424–436.
[72] M. Foex, J.P. Traverse, Investigations about crystalline transformation in rare earths sesquioxides at high temperatures, Rev. Int. Hautes Temper. Refract. 3 (1966) 429–453.
[73] M. Zinkevich, Thermodynamics of rare earth sesquioxides, Progr. Mater. Sci. 52 (2007) 597–647.
[74] L.M. Lopato, B.S. Nigmanov, A.V. Shevchenko, Z.A. Zaitseva, Interaction between lanthanum oxide and yttrium oxide, Inorg. Mater. 22 (1986) 678–681.
[75] J.L. Blanusa, M. Mitric, D. Rodic, A. Szytula, M. Slaski, An X-ray diffraction and magnetic susceptibility study of $Tm_xY_{2-x}O_3$, J. Magn. Magn. Mater. 213 (2000) 75–81.
[76] Z.K. Heiba, L. Arda, Y.S. Hascicek, Structure and microstructure characterization of the mixed sesquioxides $(Gd_{1-x}Yb_x)_2O_3$ and $(Gd_{1-x}Ho_x)_2O_3$ prepared by sol.gel process, J. Appl. Crystallogr. 38 (2005) 306–310.
[77] L. Marsella, V. Fiorentini, Structure and stability of rare-earth and transition-metal oxides, Phys. Rev. B: Condens. Matter 69 (2004) 172103–172113.
[78] C. Artini, M. Pani, A. Lausi, R. Masini, G.A. Costa, High temperature structural study of Gd-doped ceria by synchrotron X-ray diffraction ($673\,K \leq T \leq 1073\,K$), Inorg. Chem. 53 (2014) 10140–10149.
[79] C. Artini, M. Pani, M.M. Carnasciali, M.T. Buscaglia, J.R. Plaisier, G.A. Costa, Structural features of Sm- and Gd-doped ceria studied by synchrotron x-ray diffraction and μ-Raman spectroscopy, Inorg. Chem. 54 (2015) 4126–4137.
[80] A. Feteira, L.J. Gillie, R. Elsebrock, D.C. Sinclair, Crystal structure and dielectric properties of $LaYbO_3$, J. Am. Ceram. Soc. 90 (2007) 1475–1482.
[81] N. Okita, A. Higashide, M. Saito, H. Yamamura, Structure transformation between perovskite-type and B-type rare earth structures, Procedia Eng. 36 (2012) 2–6.
[82] W. Su, D. Wu, X. Ma, Q. Zhengnan, Y. Wang, X. Li, J. Zhou, D. Wang, An investigation of the effect of high pressure on the synthesis of $LaLnO_3$ compounds, Physica B+C 139–140 (1986) 661–663.
[83] A. Siaï, K. Horchani-Naifer, P. Haro-Gonzàlez, M. Férid, Effect of ytterbium substitution on $LaEr_{(1-x)}Yb_xO_3$ optical properties, J. Lumin. 172 (2016) 65–70.
[84] W.R. Gemmill, M.D. Smith, R. Prozorov, H.-C. zur Loye, Crystal growth and magnetic properties of lanthanide-containing osmium double perovskites, Ln_2NaOsO_6 (Ln = La Pr, Nd), Inorg. Chem. 44 (2005) 2639–2646.
[85] K.L. Ovanesyan, A.G. Petrosyan, G.O. Shirinyan, C. Pedrini, L. Zhang, Single crystal growth and characterization of $LaLuO_3$, Opt. Mater. 10 (1998) 291–295.
[86] K.L. Ovanesyan, A.G. Petrosyan, G.O. Shirinyan, C. Pedrini, L. Zhang, Czochralski single crystal growth of Ce- and Pr-doped $LaLuO_3$ double oxide, J. Cryst. Growth 198–199 (1999) 497–500.
[87] W. Su, L. Yang, B. Li, Optical properties and thermal stability of $LaYbO_3$ ternary oxide for high-*k* dielectric application, Appl. Surf. Sci. 257 (2011) 2526–2530.
[88] G. Vasta, A. Feteira, D.I. Woodward, D. Walker, P.A. Thomas, T.J. Jackson, Thin film $LaYbO_3$ capacitive structures grown by pulsed laser deposition, Thin Solid Films 527 (2013) 81–86.
[89] H.Y. Chen, C.L. Jia, J. Schubert, J.Q. Li, Microstructure of dielectric $LaLuO_3$ films on (0 1) SrTiO3 substrates, Thin Solid Films 517 (2008) 631–634.
[90] Y. Wang, Z. Qi, T. Shao, X. Cheng, G. Zhang, T. Li, C. Li, G. Pan, Infrared phonon modes and local structure of amorphous and crystalline $LaLuO_3$ thin films, J. Alloys Compd. 571 (2013) 103–106.
[91] M. Roeckerath, T. Heeg, J.M.J. Lopes, J. Schubert, S. Mantl, A. Besmehn, P. Myllymäki, L. Niinistö, Characterization of lanthanum lutetium oxide thin films grown by atomic layer deposition as an alternative gate dielectric, Thin Solid Films 517 (2008) 201–203.
[92] A. Vincze, R. Luptàk, K. Hušeková, E. Dobročka, K. Fröhlich, Thermal stability of $GdScO_3$ and $LaLuO_3$ films prepared by liquid injection MOCVD, Vacuum 84 (2010) 170–173.

[93] J.E. Geusic, H.M. Marcos, L.G. Van Uitert, Laser oscillations in Nd-doped yttrium aluminium yttrium, gallium and gadolinium garnets, Appl. Phys. Lett. 4 (1964) 182–184.
[94] X.-J. Liu, H.-L. Li, R.-J. Xie, N. Hirosaki, X. Xu, L.-P. Huang, Synthesis characterization, and luminescent properties of Lu_2O_3:Eu phosphors, J. Lumin. 127 (2007) 469–473.
[95] R.K. Tamrakar, D.P. Bisen, K. Upadhyay, I. Prasad Sahu, Upconversion and colour tunability of $Gd_2O_3:Er^{3+}$ phosphor prepared by combustion synthesis method, J. Alloys Compd. 655 (2016) 423–432.
[96] R.S. Yadav, R.K. Verma, A. Bahadur, S.B. Rai, Infrared to infrared upconversion emission in Pr^{3+}/Yb^{3+} co-doped La_2O_3 and $La(OH)_3$ nano-phosphors: a comparative study, Spectrochim. Acta A 142 (2015) 324–330.
[97] K. Koyabu, T. Masui, S. Tamura, N. Imanaka, Synthesis of a new phosphor based on rare earth oxycarbonate, J. Alloys Compd. 408–412 (2006) 867–870.
[98] K. Koyabu, Y. Mayama, T. Masui, N. Imanaka, Synthesis of new green emitting phosphors based on rare earth oxycarbonates, J. Alloys Compd. 418 (2006) 230–233.
[99] R. Fujiwara, H. Sano, M. Shimizu, M. Kuwabara, Quantitative analysis of UV excitation bands for red emissions in Pr^{3+}-doped $CaTiO_3$, $SrTiO_3$ and $BaTiO_3$ phosphors by peak fitting, J. Lumin. 129 (2009) 231–237.
[100] G. Seeta Rama Raju, J. Young Park, H. Chae Jung, H. Kyoung Yang, B. Kee Moon, J. Hyun Jeong, J. Hwan Kim, Synthesis and luminescent properties of low concentration Dy^{3+}: GAP nanophosphors, Opt. Mater. 31 (2009) 1210–1214.
[101] G. Blasse, Chemistry and physics of R-activated phosphors, in: K.A. Gschneidner Jr., L. Eyring (Eds.), Handbook on the Physics and Chemistry of Rare Earths, vol. 4, North Holland Publishing Company, Amsterdam, 1979, pp. 237–274.
[102] J.M. Moreau, J. Mareschal, E.F. Bertaut, Etude de $LaErO_3$ par diffraction neutronique, Solid State Commun. 6 (1968) 751–756.
[103] J. Mareschal, J.M. Moreau, G. Ollivier, P. Pataud, J. Sivardiere, Proprietes metamagnetiques de $LaErO_3$, Solid State Commun. 7 (1969) 1669–1672.
[104] J. Blanusa, M. Mitric, I. Felner, N. Jovic, I. Bradaric, The crystal structure refinement and magnetic susceptibility study of $La_{2-x}Er_xO_3$, J. Magn. Magn. Mater. 263 (2003) 295–300.
[105] T. Norby, Solid-state protonic conductors: principles, properties, progress and prospects, Solid State Ionics 125 (1999) 1–11.
[106] H. Iwahara, Proton conducting ceramics and their applications, Solid State Ionics 86–88 (1996) 9–15.
[107] H. Iwahara, T. Esaka, H. Uchida, N. Maeda, Proton conduction in sintered oxides and its application to steam electrolysis for hydrogen production, Solid State Ionics 3–4 (1981) 359–363.
[108] K.D. Kreuer, E. Schönherr, J. Maier, Proton and oxygen diffusion in $BaCeO_3$ based compounds: a combined thermal gravimetric analysis and conductivity study, Solid State Ionics 70–71 (1994) 278–284.
[109] T. Yajima, H. Kazeoka, T. Yogo, H. Iwahara, Proton conduction in sintered oxides based on $CaZrO_3$, Solid State Ionics 47 (1991) 271–275.
[110] S. Valkenberg, H.G. Bohn, W. Schilling, The electrical conductivity of the high temperature proton conductor $Ba_3Ca_{1.18}Nb_{1.82}O_{9-\delta}$, Solid State Ionics 97 (1997) 511–515.
[111] E. Ruiz-Trejo, J.A. Kilner, Oxygen diffusion and proton conduction in $La_{1-x}Sr_xYO_{3-\delta}$, Solid State Ionics 97 (1997) 529–534.
[112] E. Ruiz-Trejo, J.A. Kilner, Deuterium conductivity, diffusion and implantation in Sr-doped $LaYO_3$, Solid State Ionics 130 (2000) 313–324.
[113] V.A. Dubok, V.V. Lashneva, Yu.N. Kryuchkov, Electrophysical properties of oxide interlanthanides and solid solutions based on them, Glass Ceram. 3–4 (2003) 115–117.
[114] K. Nomura, T. Takeuchi, S. Tanase, H. Kageyama, K. Tanimoto, Y. Miyazaki, Proton conduction in $(La_{0.9}Sr_{0.1})M^{III}O_{3-\delta}$ (M^{III} = Sc, In and Lu) perovskites, Solid State Ionics 154–155 (2002) 647–652.
[115] K. Nomura, T. Takeuchi, H. Kageyama, Y. Miyazaki, High temperature crystallographic study of $(La_{0.9}Sr_{0.1})M^{III}O_{3-\delta}$ (M^{III} = Sc, In and Lu) perovskite proton conductor, Solid State Ionics 162–163 (2003) 99–104.
[116] E. Ruiz-Trejo, M.S. Islam, J.A. Kilner, Atomistic simulation of defects and ion migration in $LaYO_3$, Solid State Ionics 123 (1999) 121–129.
[117] M.S. Islam, M. Cherry, Protons in $LaMO_3$: atomistic modeling and ab initio studies, Solid State Ionics 97 (1997) 33–37.
[118] K.-D. Kreuer, A. Fuchs, J. Maier, H/D isotope effect of proton conductivity and proton conduction mechanism in oxides, Solid State Ionics 77 (1995) 157–162.
[119] W. Münch, K.D. Kreuer, St. Adams, G. Seifert, J. Maier, The relation between crystal structure and the formation and mobility of protonic charge carriers in perovskite-type oxides: a case study of Y-doped $BaCeO_3$ and $SrCeO_3$, Phase Transit. 68 (1999) 567–586.
[120] S. Coh, T. Heeg, J.H. Haeni, M.D. Biegalski, J. Lettieri, L.F. Edge, et al., Si-compatible candidates for high-κ dielectrics with the Pbnm perovskite structure, Phys. Rev. B 82 (2010) 064101.
[121] M. Olyaei, B. Gunnar Malm, P.-E. Hellström, M. Östling, Low-frequency noise in high-k $LaLuO_3$/TiN MOSFETs, Solid State Electron. 78 (2012) 51–55.